



12-2001

Numerical simulation of a crashworthy rotorcraft substructure including hard and soft surface impacts

Stephan C. Wintner

Follow this and additional works at: https://trace.tennessee.edu/utk_gradthes

Recommended Citation

Wintner, Stephan C., "Numerical simulation of a crashworthy rotorcraft substructure including hard and soft surface impacts. " Master's Thesis, University of Tennessee, 2001.
https://trace.tennessee.edu/utk_gradthes/9758

This Thesis is brought to you for free and open access by the Graduate School at TRACE: Tennessee Research and Creative Exchange. It has been accepted for inclusion in Masters Theses by an authorized administrator of TRACE: Tennessee Research and Creative Exchange. For more information, please contact trace@utk.edu.

To the Graduate Council:

I am submitting herewith a thesis written by Stephan C. Wintner entitled "Numerical simulation of a crashworthy rotorcraft substructure including hard and soft surface impacts." I have examined the final electronic copy of this thesis for form and content and recommend that it be accepted in partial fulfillment of the requirements for the degree of Master of Science, with a major in Mechanical Engineering.

Remi Engels, Major Professor

We have read this thesis and recommend its acceptance:

Gary Flandro, Roy Schulz

Accepted for the Council:


Carolyn R. Hodges

Vice Provost and Dean of the Graduate School

(Original signatures are on file with official student records.)

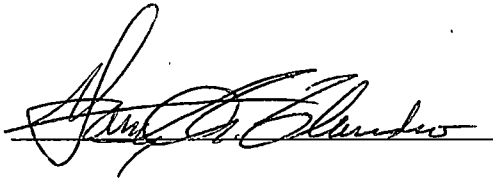
To the Graduate Council:

I am submitting herewith a thesis written by Stephan Carl Wintner entitled "Numerical Simulation of a Crashworthy Rotorcraft Substructure Including Hard and Soft Surface Impacts". I have examined the final paper copy of this thesis for form and content and recommend that it be accepted in partial fulfillment of the requirements for the degree of Master of Science, with a major in Mechanical Engineering.



Remi Engels, Major Professor

We have read this thesis and
recommend its acceptance:

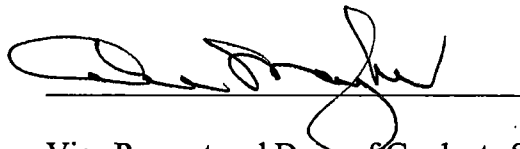


Prof. Gary Flandro



Prof. Roy Schulz

Accepted for the Council:



Vice Provost and Dean of Graduate Studies

**Numerical Simulation of a Crashworthy
Rotorcraft Substructure
Including Hard and Soft Surface Impacts**

A Thesis Presented for the
Master of Science Degree
The University of Tennessee, Knoxville

Stephan C. Wintner

December 2001

Acknowledgements

I would like to thank Dr. Remi Engels, my major professor, for his guidance and encouragment, and for arranging the facilities and giving me the opportunity to proceed with this thesis topic. I would also like to thank Dr Engels and Dr. Gary Flandro for their guidance and encouragement in the classroom.

Abstract

A design study was performed using Finite Element Analysis. The objective of the study was to demonstrate the feasibility of developing a crashworthy substructure to protect rotorcraft crew in the event of vertical impacts involving landings on both hard surfaces, for example concrete, and water or soft surfaces. Differences in the impacted surfaces behavior can change the mechanisms of loading and render hard surface energy absorption mechanisms ineffective in a water impact. The objective of this thesis was to investigate the possibility of employing a skin to transfer loads from the water to a conventional hard surface energy absorbing structure.

Finite element models were developed using the LS-INGRID preprocessor and analyzed with the LS-Dyna commercial FEA code. Use of the LS-Dyna code for simulating water impacts was validated by development of a model and comparison with experimental data in the literature. Models were developed which simulated rotorcraft substructures composed of both composites and aluminum alloys. Rotorcraft model parameters were selected based upon the Bell Helicopter model 412EP, but the model was only intended to be similar to the model 412EP, not an exact copy.

Crashworthiness was successfully demonstrated for a 26 feet per second vertical impact onto both hard surfaces and water with both the aluminum alloy and composite structures.

Table of Contents

Chapter	Page
1.0 Introduction	1
1.1 Problem Statement	2
2.0 Background.....	4
2.1 Crashworthy Structures	5
2.2 Initiators	7
2.3 Water Impact Characteristics.....	8
3.0 Theory	11
3.1 Finite Element Analysis Impact Solution Methodology	11
3.2 Element Formulations.....	13
3.3 Constitutive Relationships and Failure Criteria	14
3.4 Eulerian, Lagrangian, and Simplified Arbitrary Lagrangian-Eulerian Meshes	18
4.0 Analysis and Results	20
4.1 Introduction	20
4.2 Rigid Substructure Models - Models 1.x	22
4.3 Rigid Sphere Models - Models 2.x	23

4.4	Deformable Structure Models	26
4.4.1	Metal Substructure Models - Models 3.x	29
4.4.2	Composite Substructure Models - Models 4.x	33
5.0	Conclusion	36
	Bibliography	38
	Appendix	44
	Appendix A – Figures	45
	Appendix B – Tables	86
	Vita.....	93

List of Figures

Figure 2.1.1	Example of a FEA Model of a Vertical Sine Wave Web	46
Figure 2.2.1	Plot of the Experimentally Determined Force Displacement Curve of a Composite Sine Wave Web Beam from Zhou [34] ...	47
Figure 4.2.1	Typical Geometry For Rotorcraft Substructure Models	48
Figure 4.3.1	Model 2.16 at time $t=0.000$ sec	49
Figure 4.3.2	Sphere Center Acceleration Time History, Model 2.1	50
Figure 4.3.3	Model 2.17 at time $t=0.000$ sec	51
Figure 4.3.4	Sphere Center Acceleration Time History, Model 2.17	52
Figure 4.3.5	11-Point Centered Running Average of Sphere Center Acceleration Time History, Model 2.17.....	53
Figure 4.3.6	Experimental Sphere Center Acceleration Time History, from Pentecôte and Kindervater [25]	54
Figure 4.3.7	Sphere Kinetic Energy Time History, Model 2.17	55
Figure 4.3.8	Model 2.18 at time $t=0.000$ sec	56

Figure 4.3.9	Model 2.18 at time $t=0.005$ sec	57
Figure 4.3.10	Model 2.18 at time $t=0.009$ sec	58
Figure 4.3.11	Sphere Center Acceleration Time History, Model 2.18	59
Figure 4.3.12	Sphere Kinetic Energy Time History, Model 2.18	60
Figure 4.3.13	Pressure Plot at time $t=0.139$ Milliseconds, Model 2.18.....	61
Figure 4.3.14	Pressure Plot at time $t=0.157$ Milliseconds, Model 2.18.....	62
Figure 4.3.15	Pressure Plot at time $t=0.178$ Milliseconds, Model 2.18.....	63
Figure 4.3.16	Pressure Plot at time $t=0.199$ Milliseconds, Model 2.18.....	64
Figure 4.3.17	Sphere Center Acceleration Time History, Model 2.19	65
Figure 4.3.18	Sphere Center Acceleration Time History, Model 2.20	66
Figure 4.4.1.1	Model 3.16 at time $t=0.000$ sec	67
Figure 4.4.1.2	Model 3.16 at time $t=0.0025$ sec.....	68
Figure 4.4.1.3	Model 3.16 at Time $t=0.005$ sec	69
Figure 4.4.1.4	Floor Level Acceleration Time History, Model 3.16	70
Figure 4.4.1.5	Energy Absorption Time History, Model 3.16	71

Figure 4.4.1.6	Model 3.17 at time $t=0.000$ sec	72
Figure 4.4.1.7	Model 3.17 at time $t=0.0023$ sec.....	73
Figure 4.4.1.8	Model 3.17 at time $t=0.005$ sec	74
Figure 4.4.1.9	Floor Level Acceleration Time History, Model 3.17	75
Figure 4.4.1.10	Energy Absorption Time History, Model 3.17	76
Figure 4.4.1.11	Subfloor Beam Energy Absorption Time History, Model 3.17 ...	77
Figure 4.4.1.12	Pressure at time $t=0.0003$ sec, Model 3.17	78
Figure 4.4.1.13	Pressure at time $t=0.0005$ sec, Model 3.17	79
Figure 4.4.2.1	Model 4.7 at time $t=0.005$ sec.....	80
Figure 4.4.2.2	Floor Level Acceleration Time History, Model 4.7	81
Figure 4.4.2.3	Energy Absorption Time History, Model 4.7	82
Figure 4.4.2.4	Floor Level Acceleration Time History, Model 4.9	83
Figure 4.4.2.5	Energy Absorption Time History, Model 4.9	84
Figure 4.4.2.6	Floor Level Acceleration Time History, Model 4.10	85

List Of Tables

Table 2.0.1	Summary of Mil-Std-1290 A	87
Table 3.4.1	Summary of Linear Polynomial EOS Parameters for Simulation of Water.....	88
Table 3.4.2	Summary of Gruneisen EOS Parameters for Simulation of Water.....	89
Table 3.4.3	Summary of 2024-T4 Aluminum Alloy Material Parameters	89
Table 3.4.4	Summary of Unidirectional Carbon Epoxy Composite Material Parameters.....	90
Table 3.4.5	Summary of [0°/90°] Laminated Carbon Epoxy Composite Material Parameters	91
Table 3.4.6	Summary of [0°/90°] Laminated Kevlar Epoxy Composite Material Parameters	92

1.0 Introduction

This thesis is a numerical design study performed on a crashworthy rotorcraft subfloor structure, and the development of crashworthiness capabilities for this structure under vertical impacts onto hard surfaces, such as concrete, and water.

Due to the possibility of various helicopter rotor or engine failures, it is required that rotorcraft include some energy absorbing capability to protect the crew in the event of an accident, which often involve fairly hard vertical landings. Without such crashworthy structures, the vertical crash loads imposed upon the crew would cause severe injury, often to the spine due to the vertical direction of the acceleration. The military has sponsored a wide range of research into such structures and has developed a military standard, Military Standard 1290A (Mil-Std-1290A) [1], regarding the vertical impact velocities which rotorcraft must be able to absorb without subjecting the crew to injurious accelerations or suffering unacceptable reduction of cockpit and crew space volume.

The majority of military and civil helicopter accidents occur over water or soft soil [21]. Yet Mil-Std-1290A mainly specifies requirements for hard surface impacts. There is a soft soil impact requirement, but that is at a much lower impact speed, and hence at roughly one quarter of the impact energy specified for hard surface landings.

Comparatively little research has been performed into the simulation, analysis, and design of rotorcraft for soft surface and water impacts.

Conventional rotorcraft designs incorporate a relatively rigid semi-monocoque or monocoque structure. Monocoque structures use the skin of the structure is employed to

carry loads. The skin is often reinforced by stiffeners, making it a semi-monocoque structure. To provide crashworthiness, either the landing gear are designed to absorb energy, or under the floor of the rotorcraft are a number of structures that are intended to absorb crash energy by various deflection, crushing, and bending mechanisms. Often the landing gear are the primary energy absorbing mechanism, and Mil-Std 1290 requires a much higher vertical velocity when the landing gear are extended. If the landing gear are permanently fixed, then there may be no requirement for underfloor beams to provide crashworthiness. The beams, if present, are usually also used to help reinforce the monocoque or semi-monocoque structure. Some designs employ a truss frame design, rather than a monocoque design, which is then supplemented with landing gear or crashworthy beams. Unfortunately, all these energy absorbing mechanisms tend to rely on the impacted surface being able to sustain a number of point loads and transmit those loads to the rotorcraft. During soft surface impacts the point loaded devices, such as landing gear, are likely to be ineffective or less effective. During these impacts, the skin may be unable to transmit the distributed load applied by the soft surface to the under floor beams, and thus the entire energy absorbing mechanism may become ineffective.

1.1 Problem Statement

The objective of this thesis was to employ finite element analysis (FEA) simulations to determine the feasibility and impact on the design that would be involved in designing a skin which would effectively supplement a conventional beam structure's hard surface capabilities to allow good performance in both hard and soft surface impacts. Both metal and composite structures were studied, though the limiting case was expected to be the

composite structure, due to the brittle failure mode shown by most composites. Such failure modes do not absorb much energy, resulting in difficulty incorporating adequate energy absorption. Although the current state of the art suggests that computer simulations have not reached the stage of being a truly predictive tool [24], they do seem to show enough capability to suggest important parameters and general approaches to the problem. Therefore, the effort was directed towards producing a series of models that, while not necessarily perfectly accurate, were in the correct "ballpark" and would indicate the behavior and parameters of interest.

2.0 Background

Military Standard 1290 requirements are given in table 2.0.1. Of greatest interest are cases 3 and 7. Case 3 requires a vertical hard surface impact of 26 feet per second onto a hard surface. Case 7 is the only soft surface requirement in the specification, and is for only 14 feet per second vertically. This represents only 29% of the energy absorption required by case 3 with landing gear raised. Based upon the requirement for a 26 foot per second vertical impact with landing gear raised, the decision was made that all models must sustain a 26 ft per second vertical impact, whether over hard surfaces or water. This criterion was selected because extended landing gear were expected to have little or no effect on a water impact. The combined angle and lateral cases were of interest, but the horizontal attitude of the rotorcraft and the resulting entry effects were expected to be significant and therefore the analysis would have to incorporate them. It was expected that they would have greatly increased the model computational costs beyond the scope of this study. Therefore a simple pure vertical impact case was selected. Reference 20 incorporates an analysis considering non-vertical impact upon water, allowing an estimate of the volume of work entailed by lateral motion. Mil-Std-1290A limits permissible vertical accelerations to 20G.

Commercial FEA codes were selected as their use was common in the literature. Use of a commercially available code for the present study allows focus on the simulation and results, rather than on writing code. The commercial LS-Dyna code was selected based primarily on the recommendation of Brett Starr, a former student at UTSI who had performed similar analyses. More details of the code are included in chapter 3.

The helicopter parameters, such as weight, were loosely based on the Bell Helicopter model 412EP. This UH-1 derivative was selected as it is a common type, and therefore is interesting from a safety standpoint. Large numbers of this type suggest that it, and designs of similar size and weight such as the Sikorsky UH-60 Blackhawk, will be involved in a relatively large number of accidents, and hence a large number of personnel will be at risk in this general size and weight category, both now and in the future. It seems likely that similar helicopters will eventually be designed as replacements for the aging UH-1 derivatives. The Bell 412 was thus used to define the "ballpark" of most interest. The actual modeled structures were not intended to directly represent a Bell 412, but rather, to be similar to a real rotorcraft structure.

2.1 Crashworthy Structures

The essential problem in the design of an energy absorbing structure is to design a structure which collapses under crash loads at a rate such that the occupant is subjected to a tolerable acceleration. Depending on the direction involved, the acceleration limit varies. In rotorcraft design, Mil-Std-1290 A defines maximum acceptable limits. The energy absorbed by a structure is the area under the force-displacement curve of the structure. The area under this curve must be sufficient to absorb the kinetic energy of the vehicle in the design case of interest. A high force level will absorb the given amount of kinetic energy with a short stroke distance. High force levels, just below the acceptable limit, are desirable to minimize the stroke distance required. Reduction in stroke distance simplifies the problem of packaging the energy absorbing structure within the fuselage. To maximize the area under the force-displacement curve, this maximum allowable force

level should be sustained across the entire stroke. Peaks and valleys in the force-displacement curve are not desirable features, as they reduce the energy absorbed for a given stroke, or exceed the acceptable acceleration limits..

Energy absorbing structures of metal are usually designed in a manner such that the structure reaches its yield strength and begins to plastically deform just below the acceleration limit. From then on the metals plastically deform and absorb energy. The typical plastic behavior of metals, with low plastic moduli, allows high sustained force levels over the entire stroke to be achieved, assuming buckling failure has been avoided. In general buckling failure only plastically deforms a small volume of metal, and once the critical load has been exceeded, has a low sustained force level. Thus a structure which buckles is generally an ineffective or inefficient energy absorbing structure.

The literature has a number of papers ([8],[19],[34]) relating to the design of energy absorbing beams made of composite materials. These materials are of interest to helicopter designers due to their light weight, high strength, and often low cost of manufacture compared with conventional metal semi-monocoque structures. Further, composites often offer enhanced damage resistance and easier repair, features of great interest in the design of military combat helicopters. Composite materials do have a significant disadvantage when attempting to incorporate crashworthy structures. Their brittle failure characteristics tend to encourage sudden failure or buckling under load, rather than the plastic deformation of a metal structure. Brittle failure tends to absorb very little of the energy involved in the crash. Thus, there is significant interest in the

development of crashworthy composite structures. The military and NASA have sponsored significant research into the use of composites in crashworthy structures.

A composite energy absorbing beam concept that has received much attention is the vertically oriented sine wave web beam, Fig.2.1.1 All tables and figures may be found in the appendix. This type of sine wave web beam employs the curvature of the sine wave to provide local support and prevent a global buckling failure mode. The resulting beam absorbs energy via a variety of local fiber buckling, friction and crack propagation processes. With appropriate parameters the resulting force-displacement curve is a near ideal flat line at a force level just below the maximum allowable. This is similar to the behavior of an ideal energy absorbing structure. It was decided to proceed employing this type of vertical sine wave beam. The self-reinforcing shape seemed equally applicable to the reinforcement of conventional metals to eliminate buckling, thus forcing the beam to plastically deform over nearly its entire volume. Therefore, although the actual mechanisms producing the force-displacement curve would differ between a metal and composite structure, they would be otherwise very similar and thus allow easy comparison between them.

2.2 Initiators

The research of Farley [8] and Zhou [33],[34],[35] clearly show the need to incorporate a feature in the beam which has come to be called an initiator. Without such a feature, the force-displacement curve shows a very high peak force near the beginning of the displacement, which then falls off to a much lower force level. This initial high force is

required to cause an initial failure. Once failure has begun, the failure front propagates through the rest of the structure with much lower applied force levels. An initiator is a feature that acts like a stress concentration to cause local failure to occur at some low force level. This failed area can then propagate into the rest of the structure, and when designed well, has dramatic effects on cutting off the early force peak with minimal effect on the later force levels that provide most of the energy absorption. Many different initiators have been successfully employed in various research efforts. There was no effort to define specific initiator types in this research, as the chosen method would likely have been chosen largely on cost of manufacture. It was assumed that some viable method would be employed, and this was simulated by incorporating a row of elements that were thinner, and hence weaker, than the rest of the beam. This should produce the desired initiation of failure, and thus was felt to be adequate. An example of a near optimum force displacement curve for a composite sine wave beam from Zhou [34] is shown in figure 2.2.1. Shown in the same figure is an experimentally determined force-displacement curve of a beam without an initiator.

2.3 Water Impact Characteristics

Water or soft surface impacts show some general features of interest. The first, already mentioned, is the distributed loading applied to the entry body. Point loads cannot be sustained, and thus conventional wheeled landing gear become ineffective in water impacts. Conventional under floor beam structures will also usually become ineffective. The second issue of real concern is the "belly flop". When a blunt body enters water, the sudden application of force to the fluid over a wide area results in a very high

acceleration applied to the body. Once this force has been applied long enough to impart velocity to the fluid, the structure will sink into the water, and the force decreases rapidly. Thus the concern from a crashworthiness standpoint is to minimize and absorb the early pressure spike, presumably by crushing of the structure, and allow the fluid flow mechanisms to absorb a significant portion of the kinetic energy at later time.

Absorbing this early pressure spike suggests a need for a fairly ductile skin, which can stretch and once stretched, apply sufficient force to the existing beams to cause them to collapse and absorb some energy. Once the fluid velocity has increased and the initial pressure spike dissipated, the rotorcraft will continue down into the fluid, and dissipate energy by fluid flow mechanisms. Thus the energy that must be absorbed by the rotorcraft is significantly less than that required by a hard surface impact, even at similar impact velocities, as all energy must be absorbed by the rotorcraft structure in a hard surface impact.

To accomplish this task using metals seems a simple matter of selecting a fairly ductile metal for the skin. For example, failure strains of 20% are achievable with aluminum alloys. The concern then becomes whether that strain level will result in adequate force levels on the beams. In contrast, composites such as woven fiberglass epoxy fail at just 2.5% tensile strain. Kevlar and carbon fiber have failure strains of between 1 and 3%. Here the question of adequate ductility become a significant concern. On the other hand the stress required to fail the material is very high. Thuis and Wiggeraad [28, 29] have developed a concept called a "tensor skin" for incorporating a folded layer of polyethylene fibers behind the conventional skin structure. However, nothing has been

found in the literature that analytically shows the need for such a skin structure. Thus the composite structures are of great interest in this work.

3.0 Theory

3.1 Finite Element Analysis Impact Solution Methodology

The Finite Element Method (FEM) is a technique for the solution of a wide variety of continuum mechanics problems. As applied to structural problems, it is based upon the idea of knowing the approximate stress-strain and deflection behavior of a simple structure, such as a brick, and describing that behavior mathematically. A model of the entire complex structure is then composed of a number of such simple elements. This mathematical description can be formulated in a matrix representation of the mass and stiffness of the system. A larger and more complex system is described by assembling a series of simple systems, or elements, each of which has a mass and stiffness matrix. These matrices can be assembled into a global set of matrices that describe the entire complex system. These matrices can then be solved for deflections against a load vector by Gaussian reduction. Deflections are then related to strain and stress.

In a conventional structures problem, where the loads are either invariant or have a prescribed variation, the solution method is a simple matter of applying Gaussian reduction to the global mass and stiffness matrices. This gives a numerical solution for the deflections under load of the global system, and from the deflections of the nodes the stress state of an element may be found. The conventional modal dynamics problem is a simple determination of the eigenvalues of these matrices. These eigenvalues are in turn the natural frequencies and the eigenvectors are the fundamental mode shapes of the system. Even the more complex harmonic dynamics problem is a fairly simple extension

of the modal analysis, applying an assumed solution form to find the amplitude of the response to a dynamic excitation near the natural frequencies. This deflection response is then solved using the chosen material models to find stress states. The complexity of these analyses is found in the details of material models selection, element formulations and the construction of the finite element model. Fully integrated elements are usually employed, which is computationally expensive, but justified in the elimination of undesired mode shapes.

Unlike a conventional structures problem, the impact type problem requires a different approach. Rather than simply solving the system against a single load, or even at several time steps over a prescribed varying load, the impact problem generally requires consideration of the motion of at least two bodies, usually using conventional Newtonian mechanics, and determination of their interaction forces. These interactions then determine a significant portion of the applied loads, which are used to determine the deflections and state of stress of the system. The interaction forces and the deflections must then be fed back into the motion of the bodies, the motions integrated over time, and a new set of interaction forces determined. Then the new set of loads is applied to find a new set of deflections. Further complexity results from the non-linear material behavior that often accompanies this type of problem. This type of solution is computationally intensive, and extensive efforts are made to reduce the computational costs. For example, single-point integration of the elements is not uncommon [9], even though such elements permit undesirable hourglass modes, as the reduction in computational cost is significant. LS-Dyna and most other impact codes employ an explicit solution method. In LS-Dyna a

central difference time integration is employed to explicitly integrate from the specified initial conditions, over each time step, until the termination criteria, usually an end time, are reached [9].

3.2 Element Formulations

The Belytschko-Tsay four noded quadrilateral shell element is formulated for modeling non-linear large deflections. It is far more efficient computationally than the Hughes-Liu formulation, which is also available within LS-Dyna. The Belytschko-Tsay element employs a co-rotation coordinate velocity-strain formulation. These produce computational costs of roughly 20% those of the Hughes-Liu formulation. The primary weakness of the element is that it employs single point quadrature in the plane of the element. This permits hourglass modes to exist, which do not exist in real life.

Minimization of the hourglass mode deflection magnitudes is provided in LS-Dyna by the implementation of artificial hourglass viscosity stresses. The default method of control within LS-Dyna were used in the present study, and the LS-Post processor provides the ability to look at the hourglass energy in the model. This energy was never significant enough for concern, and therefore no effort was made to employ the alternate Englemann and Whirley control formulation, which is more computationally expensive. There is an improved version of the Belytschko-Tsay element, called the Belytschko-Wong-Chang improvement. This accounts for warpage in the element formulation, which the conventional Belytschko-Tsay shell element does not. This element was employed where possible in this research, but unfortunately showed some instabilities when applied to the modeling of sine wave beams. An element would for some reason grow to massive

strain levels without failure, which eventually caused a division by zero error. Therefore the conventional Belytschko Tsay element ended up being employed for the majority of the work. Since the skins of the modeled structure were flat, and had low out of plane warpage, this was only of concern in the sine wave beams. [9]

The 8-noded brick element form is a standard form used in almost all finite element codes. In LS-Dyna, as in the shell element, single point integration is employed to reduce computational time. This again permits hourglass modes, and again, the default hourglass viscosity control is employed. [9]

3.3 Constitutive Relationships and Failure Criteria

The Null Material (type 9) was used to represent the water. This material is efficient in that stress calculations are bypassed, and a supplied equation of state allows the resultant pressure to be defined. Although a Young's Modulus and Poisson's Ratio are input they are only used to define contact stiffness, and hence are of little concern. This material model is therefore appropriate only when material strength is non-existent, as in the case of a fluid, or of little concern, as is the case in some impact studies. Two main equations of state (EOS) were employed with the null material. The linear polynomial EOS (type 1) was used by Pentecôte and Kindervater [25]. The Gruneisen EOS (type 4) was commonly used in a set of example problems supplied along with the LS-Dyna code. Some research allowed correct parameters for both to be input into the models. The Linear Polynomial Equation of state has the form:

$$p = C_0 + C_1\mu + C_2\mu^2 + C_3\mu^3 + (C_4 + C_5\mu + C_6\mu^2)E$$

Where

$$\mu = \frac{1}{V} - 1$$

Here p is the pressure, E is the internal energy and V is the relative volume. C_1 thru C_6 are coefficients of the curve. Initial energy and volume were defined to represent no initial compression or internal energy. Parameters were set such that the fluid is a linearly compressible fluid. Parameters used with this equation of state are shown in table 3.4.1.

[9]

The Gruneisen Equation of state has the form:

$$p = \frac{\rho_0 C^2 \mu \left[1 + \left(1 - \frac{\chi_0}{2}\right)\mu - \frac{a}{2}\mu^2 \right]}{1 - (S_1 - 1)\mu - S_2 \frac{\mu^2}{\mu + 1} - S_3 \frac{\mu^3}{(\mu + 1)^2}} + (\chi_0 + \alpha\mu)E$$

Again,

$$\mu = \frac{1}{V} - 1$$

This model incorporates a cubic shock velocity - particle velocity relationship, with S_1 thru S_3 being the coefficients of the curve, and C being the intercept. Thus C is the speed of sound in the fluid. χ_0 is the Gruneisen gamma, and α is the first order volume correction to the Gruneisen gamma. Following the example files and references, a simpler linear shock velocity - particle velocity ($u_s - u_p$) relationship was used by setting the coefficients S_2 and S_3 equal to zero. Initial energy and volume were defined to

represent zero initial compression and internal energy. Parameters used with this equation of state are in table 3.4.2 [9]

Elastic Plastic (material type 3) was employed to represent aluminum. Strain hardening and strain rate effects are included in the relationship, but were not employed in this research. Parameters employed reduced the model to a simple linear elastic, linear plastic relationship with a simple maximum strain failure criteria. Parameters employed are summarized in table 3.4.3 [9]

The analysis of composite materials presents a difficulty. Unlike the isotropic behavior of metals, the macroscopic behavior of a composite is determined by the behavior of the fibers, and the matrix material. This results in different failure modes and material strengths and stiffnesses in different directions, as the fibers are oriented in a particular direction. The conventional relationship between Young's modulus, Poisson's ratio and shear modulus does not apply to a composite material. Multiple layers of fibers, with different orientations, can also be included in a composite part. Classical laminate theory assumes the global behavior of the laminate is equal to the behavior of each layer, or lamina, summed and weighted by the thickness of each lamina. For example, assuming the lamina are of identical thickness, then the behavior of a global laminate composed of two lamina would simply be the average of the behavior of the two in the direction of interest. [6]

Unfortunately, at present LS-Dyna has a limited implementation of composite elements. Material types 55, 58 and 59 are all intended to represent composite materials.

Unfortunately, types 59 and 55 are essentially identical when applied to shell elements, and neither they nor type 58 permits a shear strength in the direction normal to the shell element to be included. Material types 55 and 59 in the shell formulation are essentially assumed to represent a unidirectional material. Shear stresses and hence strength are included but are assumed to be in plane, and cross fiber shear is not considered. Failure in all three material types occurs when the material in plane strength values are exceeded or the user defined in plane strain values are exceeded. Material type 59 does permit out of plane shear considerations, and thus can represent fiber shear in a laminate, but only in a solid element. Although the use of solid elements was tried, the resulting model required an excessive amount of time to run, approaching forty hours. In this research material type 55, the Enhanced Composite Damage model, was the only composite material type used. Material type 55 does include the consideration of matrix failure, and permits the element to continue to exist after matrix failure, employing a pair of parameters to reflect the reduced strength of just the remaining fibers. [9] This material model was used to simulate composites composed of a single lamina of unidirectional Carbon Epoxy composite, two lamina of unidirectional Carbon Epoxy composite at right angles, and two lamina of unidirectional Kevlar Epoxy composite at right angles. Parameters used with this material model are shown in tables 3.4.4, 3.4.5, and 3.4.6.

The rigid material, type 20, is a conventional rigid material type. It permits no deflections whatsoever. A Young's modulus and Poisson's ratio are required for determination of contact stiffnesses, as in the null material type. Neither of these parameters are employed

in determining the stiffness matrix. The supplied density is employed to define the mass matrix. [9]

3.4 Eulerian, Lagrangian, and Simplified Arbitrary Lagrangian-Eulerian Meshes

There are two conventional approaches to the formulation of a finite element mesh. The first, the Lagrangian mesh, formulates a mesh such that the mesh nodes move with the mass being deformed. The assumed deflection mode shapes then become the basis for integration into the element mass and stiffness matrices. There is no transport of material from one node to the next. These work fine as long as deflections are small, but excessive deflections can produce poorly formed elements, with their associated numerically inaccurate results. For this reason, an Eulerian mesh is most often used to model fluid flows. The high deformation of the fluid often renders a Lagrangian mesh inaccurate after a short time. [9]

In contrast to a Lagrangian mesh, in an Eulerian mesh the nodes are stationary, regardless of the motion of the body. Mass is transported from node to node, and the mesh itself, since it does not deform, will never become poorly shaped. The assumed material velocity shapes then become the basis for integration into the element matrices. Unfortunately, the calculation of material transport is generally more costly than the computation of deflections in a Lagrangian mesh. [9]

The Simplified Arbitrary Lagrangian-Eulerian formulation combines both methods. A time step is carried out as in a conventional Lagrangian mesh. This is followed by a step involving a rezone of the mesh to correct for distorted elements. This advection step then

calculates the transportation of mass and momentum between nodes to conserve mass and energy. In a sense this is equivalent to an Eulerian formulation, where mass is transported between nodes. In LS-Dyna the rezoning algorithm is second-order accurate. The simplified ALE formulation permits only a single material per element, unlike conventional Eulerian meshes or more complex ALE meshes where multiple materials may occupy an element at the same time. This reduces computational costs. Thus the Simplified ALE formulation provides a mesh that has reduced computational cost over the conventional Eulerian mesh, and provides some protection from the poorly formed elements that can render Lagrangian meshes inaccurate. All three mesh formulations were employed in the current study, as detailed further under Section 4.0. [9]

4.0 Analysis and Results

4.1 Introduction

Four basic sets of models were created during this research. These sets can be quickly broken down into models 1.1 through 1.6, models 2.1 through 2.18, models 3.1 through 3.12 and models 4.1 through 4.14. Models 1.1 through 1.6 were rigid body models of the rotorcraft structure impacting water. Models 2.1 through 2.18 were models of a rigid sphere impacting water. Models 3.1 through 3.12 were models of a metal rotorcraft structure impacting either water or a hard surface. Models 4.1 through 4.99 were of a composite structure impacting either water or a hard surface. Each group will be described further below.

All models were created using LS-Ingrid [3] as a pre-processor, LS-Dyna [2] for analysis, and LS-Post for post-processing. All simulations were run on a Silicon Graphics "Octane" computer, in the Computational Mechanics Research Group lab.

Although it would be desirable to simulate the impact until the body comes to rest, this was not possible. Due to file space constraints and a limitation within LS-Post, it was only possible to examine approximately 128 states, or time points, during the simulation, regardless of simulation length. To obtain adequate resolution, the simulations were generally limited in length to five milliseconds, and thus the resolution of the output was .01 milliseconds. Outputs at lower resolutions would have been inadequate because the crushing of the subfloor beams happens with such rapidity. Longer overall simulations would also have required much more CPU time, and later simulations required in excess

of four hours total computational time to simulate the first five milliseconds. Pentecôte and Kindervater [25] simulated the first 20 milliseconds, and Wiggeraad and McCarthy [24] simulated the first 30 milliseconds. However, the highest acceleration peaks and general behavior of greatest interest occurred in the first 5 milliseconds of both their simulations, and also occurred in the model 2.X series described below. This can be seen in Figure 4.3.9, which was of model 2.18. These models were of rigid bodies, and ran much faster than the deformable bodies. Thus the computational cost to simulate longer times was acceptable, and reduced resolution of the output in this simulation was adequate, as great detail in the oscillatory behavior is clearly visible.

All models included gravity, and had two bodies of interest. The upper body was given an initial rigid body velocity downward, and the lower body, which represented either a hard surface or water, was stationary. Symmetry planes, if used, were the only constraint applied to the bodies paths. The initial separation between the bodies was very small, to minimize computation time, but the bodies were not initially touching.

Contact algorithms were employed between the bodies. LS-Dyna permits several types of automatic contact routines, and automatic one-way surface to surface (type a10) and automatic surface to surface (type a3) contacts were employed. These routines automatically insert contact elements as required between two defined materials, eliminating the tedious and often difficult task of manually applying contact meshes.

Although rotorcraft often incorporate further energy absorbing protection for the crew such as seats which collapse under a 20G load, this ancillary equipment was not

considered in the analysis. Thus sustained accelerations above 20G at the floor level were regarded as unacceptable. Attempts were made to minimize any acceleration at the floor level above 20G. It was assumed that very brief accelerations above 20G would be absorbed by supplementary energy absorbing means.

4.2 Rigid Substructure Models - Models 1.X

Models 1.1 through 1.6 were used largely for learning to use LS-Dyna. They employed a rigid helicopter substructure that was similar to the intended final geometry. This model was used to conduct some basic mesh sensitivity studies and effectively learn how the software works.

All rotorcraft structure models employed an initial geometry similar to figure 4.2.1. The structure is traveling in the negative Y direction, as are all models.

Since the structure was rigid, acceleration levels were very high. There was a consistent early peak, followed by a gradual decay at much lower levels. This is indicative of the "belly flop" pressure pulse described earlier. The deformable models discussed later have as their primary goal the attenuation of the peak to tolerable levels. This behavior is very similar to that of the rigid sphere models described in the next section.

These models are of little further interest, and hence no further description will be given.

4.3 Rigid Sphere Models - Models 2.X

Models 2.1 through 2.18 modeled a rigid sphere plunging into water. The accelerations at the center of the sphere were compared with data in Pentecôte and Kindervater [25]. The intent was to demonstrate the accuracy and feasibility of using LS-Dyna for water impact analyses, and to validate the equations of state and mesh density chosen for use to represent water. Sphere size, impact velocity and weight were given in the reference.

A rigid sphere of 8-noded rigid brick elements (material type 20) was employed, and dropped into a body of water that was 2.5 diameters on a side, as in Fig 4.3.1, or 2.25 radii on a side, as in fig 4.3.3. Some models employed 1/4 symmetry planes to reduce model size and computation time. Since the data was for an impact velocity of 11.8 meters per second all models employed an initial vertical velocity of 464 inches per second in the negative Y direction. Density and diameter of the sphere was derived from given values of 0.251 meter diameter and 3.76 kilogram mass, converted to appropriate units.

The water was represented by a mesh of 8-noded brick elements with a null material type. As stated before, two equations of state (EOS) were employed with the null material type. Models 2.17 and 2.18 are identical except for the EOS used. Model 2.17 employed the linear polynomial EOS, and model 2.18 employed the Gruneisen EOS. Both produced essentially the same results, shown in figures 4.3.4, 4.3.7, 4.3.11, and 4.3.12. Images of Model 2.18 before and during impact may be seen in figs 4.3.8, 4.3.9 and 4.3.10, and Model 2.17 has visually identical behavior. Note the large displacements and splashing

"fold over" effects occurring in the elements near the sphere. The linear polynomial EOS was used throughout the rest of the work for consistency.

This series of models was also used to validate the use of symmetry. Models 2.16 and 2.17 are identical in all parameters except that model 2.17 is a one quarter symmetry model. See figs 4.3.1 and 4.3.3. They produced identical output, figs 4.3.2 and 4.3.4.

This set of models was also used to conduct a comparison between the Lagrangian, Eulerian, and Arbitrary Lagrangian-Eulerian formulations [9]. Models 2.19, 2.20 and 2.17 employed each formulation, respectively, with a linear polynomial EOS. Their results were identical, figs 4.3.17, 4.3.18 and 4.3.4. The Lagrangian and ALE formulations ran faster than the Eulerian formulation. Since the ALE formulation ran fast and provided some safety from poorly formed elements, it was used for all subsequent models.

Returning to figures 4.3.8, 4.3.9 and 4.3.10, note the large displacements and splashing "fold over" effects occurring in the elements near the sphere. This suggests that the use of a purely Lagrangian formulation would be likely to produce erroneous results due to the distorted shapes, though it does not appear to have had an appreciable effect on the acceleration of the sphere center.

Mesh sensitivity studies were also performed using these models, and demonstrated little sensitivity to sphere or impacted fluid mesh density.

Unfortunately, these models consistently overpredicted the accelerations involved, when compared with data in Pentecôte and Kindervater. Figures 4.3.4 through 4.3.6 consist of a plot of the acceleration at the center of the sphere, a plot of the eleven point centered

running average of the acceleration data in the previous figure, and the experimental data from Pentecôte and Kindervater. Peak accelerations from model 2.18 was 113 G, compared with a peak of roughly 68 G in Pentecôte and Kindervater. However, the simulations had a highly oscillatory behavior not present in the data. Since the sphere is rigid, this cannot be due to the sphere vibrating, and even taking an 11 point centered running average produces a curve that is visually nearly identical, with the same highly oscillatory behavior present. However, the peak acceleration of the averaged data is 95.1 G, which compares significantly better. The data given in Pentecôte and Kindervater was filtered, and very little description was given of the filtering process. The sharply oscillatory nature of the numerical response may indeed have existed in the experiment, and been filtered out, if indeed the experimental instruments could have detected it. Alternately, it may have been an artifact of the simulation. However, if it was an artifact of the simulation, then it should have shown some sensitivity to the mesh density, which it did not. The averaged curve shows a close match to the general shape of the curve in the data, with the exception of a pair of very sharp, short duration peaks near 4.25 and 5.8 milliseconds. But these peaks may have existed and been filtered out. Although the model could probably have been more closely matched to the data by employing a lower than correct density, this was not done. Concern over the understanding of the data led us to continue using material parameters that were understood based upon other references. However, this discrepancy is of significant concern.

A probable mechanism for this sharply oscillatory behavior can be seen in figures 4.3.13 through 4.3.16. These images of the pressure in the fluid near the sphere entry show a

sharp oscillation in the maximum pressure at the contact region between the sphere and the water, swinging wildly over very short time steps. This changing pressure would of course have been directly transmitted to the rigid sphere as a changing force, and hence to a changing acceleration. The contact appears to produce a pressure wave, which then propagates rapidly away from the contact region. As the energy of the wave is spread over a rapidly increasing volume, it rapidly dissipates and ceases to impart significant momentum to the fluid. The fluid nearest the sphere receives the most momentum and thus the contact pressure drops off, since the relative velocity between the sphere and fluid decrease. The fluid then begins to compress against nearby fluid that received less momentum, and the sphere itself is coming into contact with more fluid which was further away from the first pressure wave and has less momentum. Thus the fluid at the sphere contact area has a rapidly oscillating relative velocity, and of course the relative velocity drives the pressure up and down. Examples of very similar behavior can be seen in figures 4.4.1.12 and 4.4.1.13, which are of rotorcraft substructure models. Some further discussion of those images can be found in chapter 4.4.1.

4.4 Deformable Structure Models

Models 3.x and 4.x are very similar, and some common features will be mentioned here. Both employed a deformable vertical sine wave beam, with an initiator. The initiator was defined as a horizontal row two elements tall along the beam that have thinner shell thickness, and therefore are likely to buckle first. General geometry can be seen in fig 4.4.1.1. Note the initiator near the bottom of the sine wave beam. Four underfloor beams, evenly spaced on either side of the centerline, were chosen. Concern over the potential

skin shear failure mode seemed to suggest that a distributed underfloor structure would perform better, compared with a structure employing a single keel beam or a pair of beams.

Models 3.x and 4.x both employed a rigid floor, with a density and thickness which together gave a weight representative of the average weight per unit area of the Bell 412EP. A Bell 412EP has a maximum gross take off weight (MGTOW) of 11900 lbs and a fuselage length of roughly 11 feet [32]. 11,000 lbs was assumed to reside in the fuselage. Thus the weight is 83 pounds per inch of fuselage length. Spread over a width of 100 inches, also taken from the Bell 412EP, this leads to an average weight of 0.83 lbs/square inch, and hence to a density for the floor of 1.66 pounds per cubic inch with a thickness of .500 inches. Symmetry planes were applied to the front and rear XY planes, and the center YZ plane. This thus represents a condition in the center of the fuselage, away from the ends.

With the exception of models 3.1 through 3.3, all models employed a radius for the sine wave of .750 inches. The early models disclosed a need for a tighter radius. Zhou [34] employed a beam 3 inches tall and used a .750 inch radius. Models 3.1 through 3.3 employed a radius of 3 inches, based on a 4x scaling of Zhou's beams to achieve the 12 inch height. It seems the beam radius is driven largely by shell thickness, and is unrelated to the height of the web. This parameter, which may be important for achieving optimal beam performance, was not iterated further, as the goal of the thesis was not to optimize the beam more than required to achieve adequate hard surface energy absorption.

Iterations of the beam shell thickness and initiator thickness allowed acceptable energy absorption to be achieved using a .750 inch radius in model 3.16.

The hard surface impacts were simulated by setting the body underneath the rotorcraft structure to rigid material (type 20) and fixing the bottom surface. In other models, the same body was set to material type 9, employing a linear polynomial equation of state, and an ALE formulation, to simulate water. A non-reflecting boundary condition was applied on the bottom and outside faces of the water to simulate the effect of a large body of water. This condition permits pressure waves to propagate outside the simulated domain, and permits the water to advect out of the model if predicted by the ALE formulation.

Both models employed a 4 noded Belytschko-Tsay shell element throughout for the rotorcraft substructure. The Belytschko-Wong-Chang improvement was used for the vertical sine wave webs, except for the initiator. This was due to instability caused by using the Belytschko-Wong-Chang improvement in the initiators, as mentioned earlier. The choice of element was based upon several references which suggested that although the Belytschko-Tsay shell incorporates some incorrect hourglass modes, this element represented the optimum way to reduce computation times, because it is computationally efficient. Unfortunately, the long run times and large files required by even this formulation prevented the comparison with more computationally expensive alternate formulations.

Due to the contact algorithms employed, and the shape of the geometry, there was a need to model rigid footings under the beams. These footings were only slightly wider than the beam, and were of rigid material (type 20). These footings allowed nodes to be positioned in such a fashion that a good join existed between the sine wave beams and the floor, and still permitted nodes to be placed directly above the grid pattern of the water, thus avoiding interpenetration difficulties. Otherwise the contact algorithm was unable to identify the nodes to apply contact equations between, since their horizontal plane separation was too great. This resulted in incorrect penetrations occurring in the simulation. Since the subfloor beams must be in some fashion joined to the skin, the existence of a flange in a real world design is likely, and this was not felt to be a significant compromise in the usefulness of the model. This flange would likely be used for riveting or bonding the skin in a metal or composite structure, respectively.

The interfaces between the various materials in the structure were joined by the simple expedient of merging coincident nodes. This has the effect of treating all these joints as perfectly bonded joints, capable of failure only if the joined material would fail.

Modeling these joints with better fidelity would substantially increase the computational costs associated with this analysis. Since the joints are well understood technology, and are not the focus of this research, no effort was made to incorporate higher fidelity joints.

4.4.1 Metal Substructure Models - Models 3.X

The aluminum structure models (Models 3.x) employed a plastic kinematic material model, type 3 in LS-Dyna, for the beam and skin structure. The skin parameters and

beam parameters were both based on 2024-T4 aluminum. 2024-T4 is a commonly used high strength aluminum alloy. 7075-T6 is another common alloy, and the only common alloy which is significantly stronger, but has other undesirable qualities. 2024-T4 was selected based on its high strength, high ductility, and good weldability and formability. There is no reason to believe that a crashworthy structure made of 7075-T6 would perform poorly, assuming the structure was properly designed, but the structure would likely be more difficult and more expensive to manufacture, as welding or forging is likely to be employed in fabrication. 7075-T6 is often used for skins, but its lower ductility suggests difficulties, and hence 2024-T4 was again chosen. Material data was obtained from www.matweb.com [4] and confirmed by several other sources. These parameters are summarized in table 3.4.3.

One parameter that was varied in numerical studies was the vertical location of the initiator, and the vertical size of the initiator. They were varied in an effort to eliminate the early spike in the force-displacement curve. A number of different locations were tried. Unfortunately, none produced an ideal force-displacement curve. Model 3.16 has the initiator located at the bottom of the web, between 2.5 and 3.5 inches above the skin. It appears that the effectiveness of the initiator is enhanced by being located in an area near the bottom of the beam where contact with the ground applies high localized stresses. However, if the initiator is located too low, it has little effect. Because the initiator was not the focus of this research, no effort was made to understand the effect of initiator position in a more thorough manner.

Model 3.16 performed reasonably well in a hard surface impact, figures 4.4.1.1 through 4.4.1.5. The floor level accelerations show an unfortunate early spike, which is higher than the permissible 20 G, and accelerations at later times that are well below the permissible 20G. However, with this model it was difficult to iterate design parameters to eliminate the spike and produce good energy absorption. The final design is the best compromise available, and the incorporation of energy absorbing seats seems likely to render this design acceptable, because the seats would attenuate the early spike. The initiator was 0.015 inches thick, and the rest of the beam was 0.020 inches thick. It appears that although the beam and initiator thickness have a large influence on the early peak, they have less on later force levels. It seems that once initial local buckling has occurred, the post-buckling force levels are not heavily influenced by beam thickness and are probably more influenced by items such as sine wave radius. Iteration and understanding of the beam behavior was not a focus of the research, and so this was not pursued. Model 3.16 had reached the stage of being a reasonable approximation of the hard surface capable subfloor structure.

Regarding water impacts, Model 3.17 is identical to Model 3.16 except that the impact surface material and equations of state were changed to represent water. Model 3.17 achieved adequate attenuation of the initial force peak with a ductile skin, which stretched to absorb the early pressure peak, with some crushing of the beams. The total energy absorbed, nearly 11,000 lbf-in, was significantly better than the 7592 lbf-in performance of Model 3.16 over the same time span. The underfloor beams absorbed approximately 1/2 of the total energy absorbed, less than in Model 3.16 over the same

time span, as shown in figures 4.4.1.6 through 4.4.1.13. The skin was only 0.015" thick, and although a thicker skin could be included, the floor level accelerations would be higher, and the design would have excess weight. Note that in figure 4.4.1.7 the skin between the beam has only deformed near the edges of the footings under the beams. The skin near the middle does not stretch and deform until closer to the end of the impact condition, figure 4.4.1.8.

In figure 4.4.1.12 note the two regions of very high pressure. These began underneath the subfloor beams, and have propagated away from the structure. The "softer" areas between the beams have produced almost no pressure spike up to this time. This suggests the need for a thicker skin, or footing, near the region of structures, such as the beam, which attempt to apply point loads and are relatively stiff in the direction normal to the water surface. A thinner skin may be employed successfully away from such point load structures. As these are useful from a manufacture point of view as well, this is encouraging. In figure 4.4.1.13 the continued propagation of the initial entry pressure wave may be seen, as well as the development of a secondary pressure wave. This oscillatory surface pressure accounts for much of the oscillatory nature of the floor level acceleration-time curve. As can be seen in figure 4.4.1.11 the plastic deformation energy absorbed by the beam continues to increase throughout the simulation, and is already significant at 2.3 milliseconds. In fact, at very early times it appears that it may represent most of the energy absorbed. This suggests that the subfloor beams play a substantial role in absorbing the initial pressure spike, and that a subfloor beam (or other subfloor structure) which has an overly high initial buckling load may have a very high initial

peak floor level acceleration, regardless of skin design. The skin behavior would appear to have more influence on later time accelerations. Recall that the beams employed here already have an overly high initial failure load. However, this suggests that the potential shearing failure of the skin near the beam is quite important. If the skin were to experience this type of failure during initial entry, when the shear load is at the highest locally and the skin is not yet fully loaded, the beams would be unable to absorb the initial pressure spike. Tensile rupture of the skin at later times may be less of a problem, as the pressure has already imparted some velocity to the local fluid. This suggests that the use of 7075-T6, which has a lower tensile ductility but a higher shear strength than 2024-T4, may allow the design of a more effective structure from both a vehicle weight and crashworthiness capability standpoint.

4.4.2 Composite Substructure Models - Models 4.X

Composite structure models (Models 4.x) employed material model type 55 for the beams, and for the skin. Model 55 is intended for use with unidirectional fiber composites. As these are the primary load bearing members, this was felt to be reasonable. The Kevlar skins employed by Wiggensraad and McCarthy [24] are difficult to simulate in LS-DYNA, as it lacks a multi-lamina material model. Nonetheless, type 55 was employed with parameters input to represent a pair of unidirectional carbon-epoxy lamina, one with fibers in the X direction and one with the fibers in the Z direction, as well as with parameters representing a single unidirectional carbon-epoxy lamina. Parameters are shown in Tables 3.4.4, 3.4.5, and 3.4.6.

Parameters representing a simple unidirectional laminate beam were employed, with the fibers were oriented in the Y direction. These models consistently failed to behave in a manner representing the experimental data given by Zhou [34] and Wiggenraad and McCarthy[24]. See figures 2.2.1, 4.4.2.1 and 4.4.2.2. Note the high peaks, and the low sustained acceleration. In comparison, data from Zhou and Wiggenraad and McCarthy have no early peaks, and a higher sustained crush load. However, the thickness of Wiggenraad and McCarthy's and Zhou's beam is much thicker than that employed in the current work. As a result, the force required to initiate and sustain crushing would produce excessively high accelerations using the floor weighting used in the current work. Perhaps some different mechanisms become significant in such thin beams, or perhaps the modeling employed in the current work is insufficient to capture such behavior accurately. In both reference works, the beams employed in their research were composed of a unidirectional carbon epoxy lamina core, with a woven Kevlar skin surrounding it. The Kevlar skin was ignored in the current work, due to the limitations of the available material models. Adjustment of parameters, primarily beam and initiator thickness, allowed a reasonable beam behavior to be developed, but these models did not predict the sustained high crush loads without peaks which both Zhou and Wiggenraad and McCarthy demonstrated experimentally. Note that both the aluminum and composite beams developed in the current work had very similar behavior and energy absorbing performance. In spite of the sub-optimal beam behavior, the beams had again reached the point of being a reasonable energy absorbing structure, and so attention was turned to the water impact case.

Based on the beams of model 4.7, model 4.9 was created. The composite skins of model 4.9 were based upon two layers of unidirectional carbon fiber / epoxy composite, one layer running in the global X direction and the other in the global Z direction. As before, the linear polynomial EOS with a null material was employed to simulate water. This skin showed good performance in the water impact case and did not suffer the expected tensile failure, figures 4.4.2.3 through 4.4.2.5. Elastic growth of the skin to near failure did occur however. This suggests that significantly higher vertical impact velocities might cause brittle tensile rupture. Floor level accelerations were very similar to Model 3.17, but slightly higher. This may well be due to the higher stiffness of the composite skin in comparison to the aluminum skin of model 3.17. Unfortunately, this model cannot correctly evaluate the possibility of shear failure occurring near beam footings, due to the inherent limitations of the material model. Model 4.10 employed parameters to simulate a more ductile skin composed of two layers of unidirectional Kevlar, but was otherwise identical to model 4.9. This Kevlar skin also performed well, see figures 4.4.2.4 through 4.4.2.7. In both models 4.9 and 4.10, the overall behavior was visually very similar to model 3.17, and hence figures are not provided.

5.0 Conclusions and Recommendations

Although these numerical studies are of somewhat questionable accuracy, and require validation before the results may be regarded as definitive, this study suggests some significant behaviors, trends and design parameters of concern.

The results lead to the conclusion that moderate water impact capability is easily achievable in a fairly conventional helicopter structure of either composite or metal materials. In fact, it should be quite possible to design a structure that has more energy absorption capability than the same design for hard surface impacts. Skins employed in this research were able to transmit distributed water loads to the subfloor beams rather easily, with minimal impact on the design. Further research into the magnitude of the pressure pulse created by higher impact speeds, such as the 42 feet per second required with landing gear extended, is indicated. Note that a underfloor beam structure such as that employed herein, with four beams across the width, is more likely to support the skin and perform well than a design using a single beam, or pair of beams. Designs including only a single beam would presumably require a more complex skin design to provide adequate performance.

The composite skins employed in this work approached their tensile failure limits, though they did not exceed them. This suggests that significantly higher speeds would be likely to cause tensile rupture of the composite skins. Tensor skin concepts such as those advanced by Thuis and Wiggeraad [28,29] would likely be required if water crashworthiness capability was to be extended to the 42 feet per second required for an

extended landing gear hard surface impact. Limits for metal skins appear to be somewhat higher, in spite of the higher strength of composites.

This study also suggests that post-water impact survival has much to do with easy egress while in or under water, crew personal flotation devices and so forth, as the vehicle is likely to plunge rather deeply into the water before bleeding off vertical velocity.

Difficulties with adjusting parameters to eliminate the spikes in the force displacement curve suggest that the modeling of initiator features employed in this research are not adequate, and more research might be performed to determine a better approach to incorporating such features. The difficulties encountered when comparing the rigid sphere water impacts with the data of Pentecôte and Kindervater [25] suggest further validation of the water modeling methodology is required.

Further, the limited ability of the composite materials available in LS-Dyna to simulate the desired geometry suggest that new material models would be highly desirable.

Specifically, a model incorporating the ability to specify stiffness and strength in all three directions, including initial matrix and ultimate fiber failure regions, implemented for shell elements as well as solid elements, would be highly desirable. Ideally this element would permit definition of properties of each individual lamina, synthesize global laminate properties from the input lamina parameters and incorporate a progressive lamina by lamina failure model.

Bibliography

1. Anon., "Military Standard : Light Fixed Wing and Rotary-Wing Aircraft Crash Resistance", MIL-STD-1290 A, United States Department of Defense, Washington DC September 1988
2. Anon., "LS-Dyna User's Manual : Nonlinear Dynamic Analysis of Structures", Livermore Software Technology Corporation, May 1999 Version 950
3. Anon., "LS-Ingrid: A Pre-Processor And Three-Dimensional Mesh Generator For The Programs LS-DYNA,LS-NIKE3D, And TOPAZ3D", Livermore Software Technology Corporation, Version 3.5, August 1998
4. Anon., "Matweb : The Online Materials Information Resource",
<http://www.matweb.com/>
5. Bolukbasi, A.O., "Development of an Analysis Methodology for Crash Impacts on Soft Soil", Proceedings of the 54th American Helicopter Society Forum, Washington D.C., May 20-22, 1998
6. Daniel, I.M., and Ishai, O. Engineering Mechanics of Composite Materials, Oxford University Press, New York New York, 1994
7. Delasart, D., Deletombe, E., Kohlgrueber, D., Johnson, A., "Development of Numerical Tools for the Simulation of Composite Helicopter Structures" Proceedings of the 56th American Helicopter Society Forum, Virginia Beach VA, May 2-4, 2000
8. Farley, G.L., "Energy Absorption of Composite Material and Structure", Proceeding of the 43rd American Helicopter Society Forum, St. Louis Mo, May 18-20, 1987

9. Hallquist, J.O., "LS-Dyna Theory Manual", Livermore Software Technology Corporation, May 1998
10. Hashish, E., Sareen, A.K., Smith, M.R., "Crash Analysis of an Energy-Absorbing Subfloor During Ground and Water Impacts", Proceedings of the 55th American Helicopter Society Forum, Montréal, Québec, May 25-27, 1999
11. Jackson, K.E., and Fasanella, E.L., "Impact Testing and Simulation of a Crashworthy Composite Fuselage" Proceedings of the 56th American Helicopter Society Forum, Virginia Beach VA, May 2-4, 2000
12. Jackson, K.E., Fasanella, E.L., Kellas, S., Boitnott, R.L., "Full-Scale Crash Test of the Sikorsky Advanced Composite Airframe Program Helicopter" Proceedings of the 56th American Helicopter Society Forum, Virginia Beach VA, May 2-4, 2000
13. Jackson, K.E., Fasanella, E.L., Lyle, K.H., "Finite Element Simulation of a Full-Scale Crash Test of a Composite Helicopter", Proceedings of the 56th American Helicopter Society Forum, Virginia Beach VA, May 2-4, 2000 Forum, Virginia Beach VA, May 2-4, 2000
14. Jackson, K.E., Fasanella, E.L., "Crashworthy Evaluation of a 1/5 Scale Model Composite Fuselage Concept", Proceedings of the 55th American Helicopter Society Forum, Montréal, Québec, May 25-27, 1999
15. Jackson, K.E., Fasanella, E.L., Lyle, K.H., "Development of an ACAP Helicopter Impact Model", Proceedings of the American Helicopter Society National Technical Specialists Meeting on Rotorcraft Crashworthiness, Phoenix AZ, September 14-16, 1998

16. Jackson, K.E., Fasanella, E.L., Lyle, K.H., "Crash Simulation of an Unmodified Lear Fan Fuselage Section Vertical Drop Test", Proceedings of the 54th American Helicopter Society Forum, Washington D.C., May 20-22, 1998
17. Jackson, K.E., Fasanella, E.L., "Innovative Composite Fuselage Design for Improved Crashworthiness ", Proceedings of the 54th American Helicopter Society Forum, Washington D.C., May 20-22, 1998
18. Jackson, K.E., Kellas, S., Kindervater, C., Lützenberger, M. "Experimental and Simulated Crash Response of Composite Airframe Structures", Proceeding of the 50th American Helicopter Society Forum, Washington D.C., May 11-13, 1994
19. Johnson, A.F, Kindervater, C.M., Jackson, K.E., "Multifunctional Design Concepts for Energy Absorbing Composite Fuselage Sub-Structures", Proceedings of the 53rd American Helicopter Society Forum, Virginia Beach VA, April 29-May 1, 1997
20. Johnson, A.F, Kindervater, C.M., Kohlgrueber, D., Lützenberger, M., "Predictive Methodologies for the Crashworthiness of Aircraft Structures", Proceedings of the 52nd American Helicopter Society Forum, Washington D.C., June 4-6 1996
21. Kinker, L.E., Loeslin Jr., G.F., Contarino, R., "U.S. Naval and Marine Corps Helicopter Mishap Trends : Does the Past Offer Help for the Future ?", Proceedings of the 53rd American Helicopter Society Forum, Virginia Beach VA, April 29-May 1, 1997
22. Kinslow, R., High Velocity Impact Phenomena, Academic Press, London 1970
23. Kohlgrueber, D., Kamoulakos, A., "Validation of Numerical Simulation of Composite Helicopter Sub-Floor Structures Under Crash Loading", Proceedings

of the 54th American Helicopter Society Forum, Washington D.C., May 20-22, 1998

24. McCarthy, M.A., Wiggenraad, J.F.M. "Numerical Investigation of a crash test of a composite helicopter subfloor structure", Composite Structures 51, 2001
25. Pentecôte, N., Kindervater, C.M., "Airframe Water Impact Analysis Using a Local/Global Methodology", Proceedings of the 55th American Helicopter Society Forum, Montréal, Québec, May 25-27, 1999
26. Richards, M.K., Kelley, E.A., "Development of a Water Impact Dynamic Test Facility and Crash Testing of a UH-1H Aircraft onto a Water Surface", Proceedings of the 55th American Helicopter Society Forum, Montréal, Québec, May 25-27, 1999
27. Shin, Y.S., Zukas, J.A., "Structures Under Extreme Loading Conditions", PVP-325 ASME, New York 1996
28. Thuis, H.G.S.J., deVries, H.P.J., Wiggenraad, J.F.M., "Sub-Floor Skin Panels for Improved Crashworthiness of Helicopters in Case of Water Impact", Proceeding of the 51st American Helicopter Society Forum, Fort Worth TX, May 9-11, 1995
29. Thuis, H.G.S.J., and Wiggenraad, J.F.M., "A Tensor Skin Concept for Crashworthiness of Helicopters in Case of Water Impact", Proceeding of the 50th American Helicopter Society Forum, Washington D.C., May 11-13, 1994
30. Wittlin, G., Schultz, M., Smith, M.R., "Rotary Wing Aircraft Water Impact Test and Analyses Correlation", Proceedings of the 56th American Helicopter Society Forum, Virginia Beach VA, May 2-4, 2000

31. Wittlin, G., Smith, M.R., Sareen, A., Richards, M., "Airframe Water Impact Analysis Using a Combined MSC/DYTRAN - DRI/KRASH Approach", Proceedings of the 53rd American Helicopter Society Forum, Virginia Beach VA, April 29-May 1, 1997
32. Wyatt, D., Bell 412 EP Sales Brochure, Bell Helicopter Textron Inc., Fort Worth TX, January 2000
33. Zhou, W., Hanagud, S., Craig, J.I., , "Crashworthy Behavior of Graphite/Epoxy Composite Sine Wave Webs", AIAA 91-1196-CP
34. Zhou, W., "Crash-Impact Behavior of Graphite/Epoxy Sine Wave Webs", Ph. D. Thesis, Georgia Institute of Technology, November 1989
35. Zhou, W., Hanagud, S., Craig, J.I., Sriram, P. , "Energy Absorption Behavior of Graphite/Epoxy Composite Sine Webs", Journal of Composite Materials, May 1989
36. Zukas, J.A., High Velocity Impact Dynamics, John Wiley&Sons, New York 1990
37. Zukas, J.A., Nicholas, T., Swift, H.F., Greszczuk, L.B., Curran, D.R., Impact Dynamics, John Wiley&Sons, New York 1982

Appendix

Appendix A - Figures

Such a web would be sandwiched between the floor skin of a rotorcraft and intended to absorb energy by being crushed in a direction parallel to the axis of the corrugations.

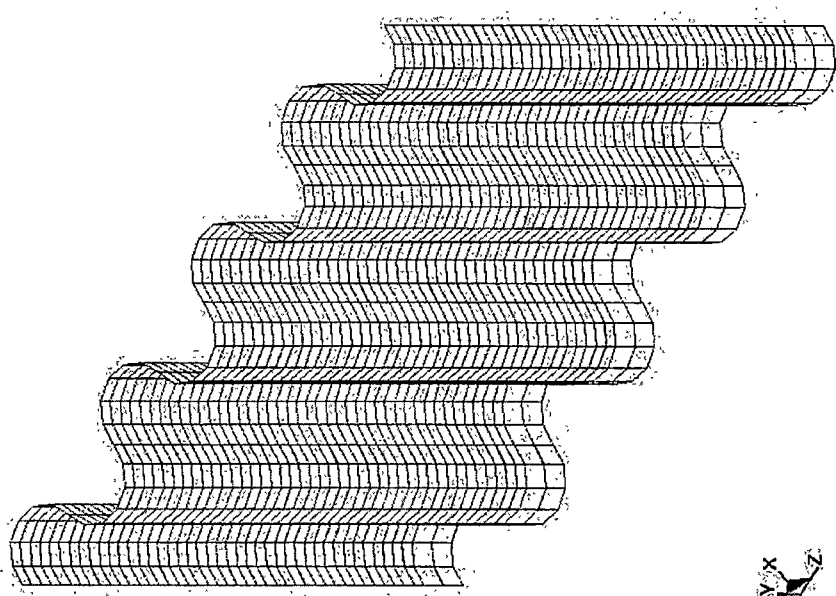


Figure 2.1.1 Example of a FEA Model of a Vertical Sine Wave Web

These beams were composed of a unidirectional Carbon Epoxy core, with the two outermost lamina composed of woven Kevlar. Note the effect of the initiator. Also note the high sustained crush load of beam b. The beam was only 4.5 inches in length, compared with 12 inches in the current study. Hence the 20 kN load of Zhou's beam would be equivalent to 53.3 kN in the current study, for each beam. The two beams together would apply a 48.12 G load to the 498 pound floor in the current study. Thus Zhou's beam is overly stiff for the current study by a factor of roughly 2.5.

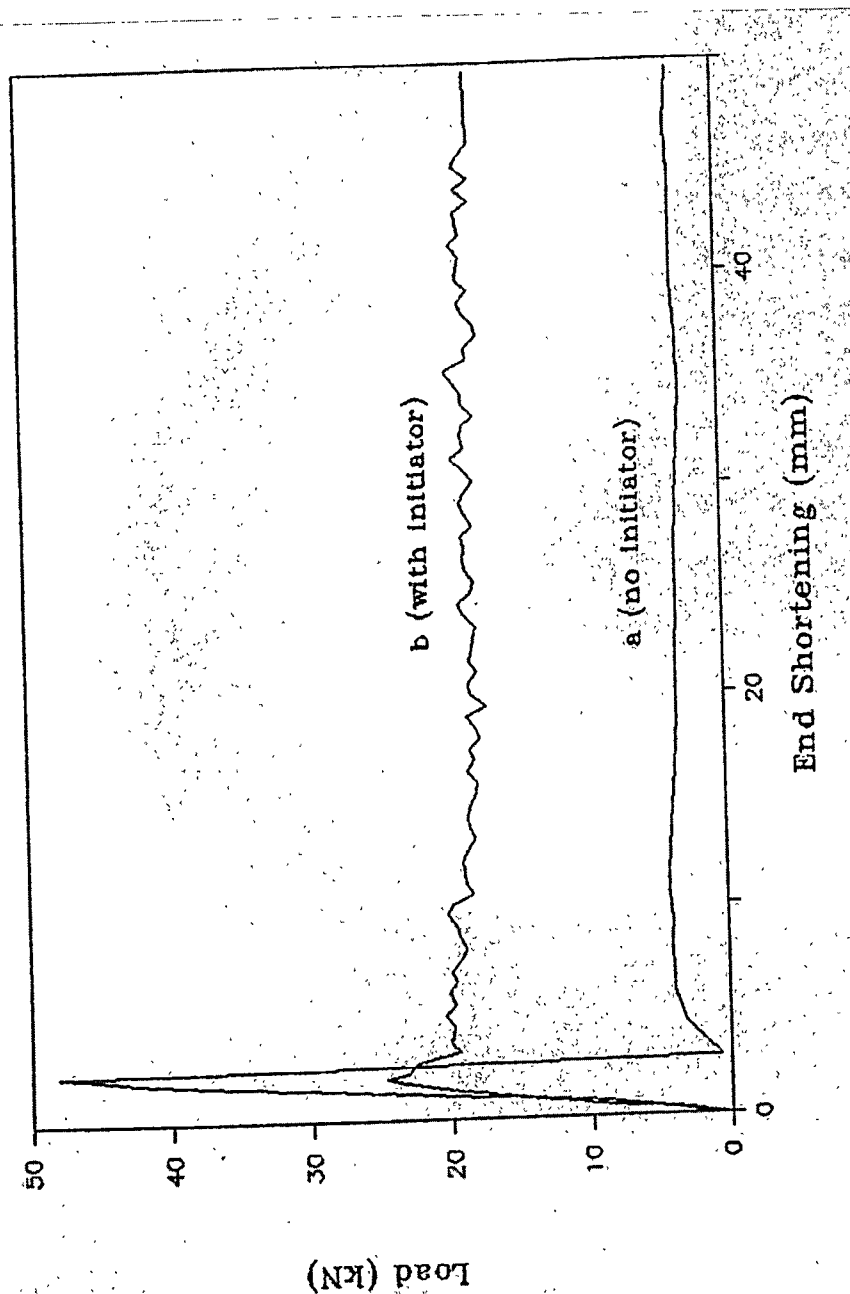
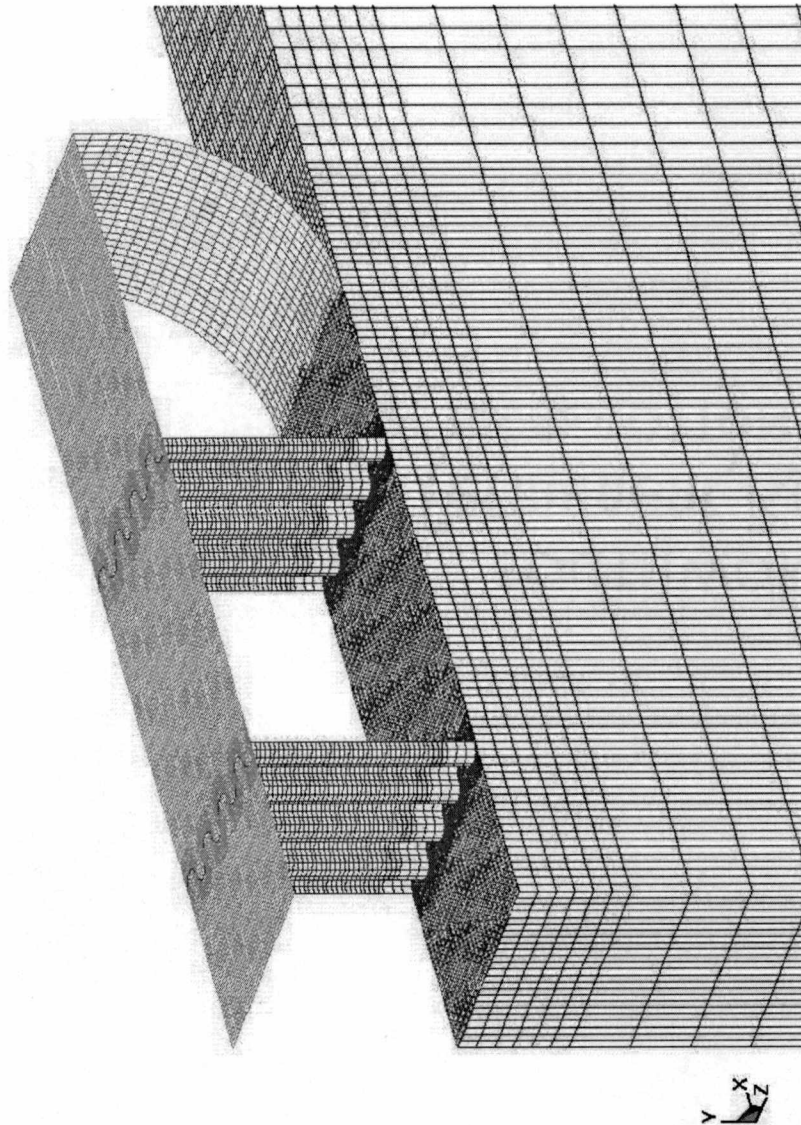


Figure 2.2.1 Plot of the Experimentally Determined Force Displacement Curve of a Composite Sine Wave Web Beam from Zhou [34]

3D MODEL 3.16, PLASTIC FAILURE AL
Time = 0



Rotorcraft substructure consists of two sine wave web beams, the rotorcraft floor, and the skin. Underneath the substructure can be seen the impacted body. In some cases this body represents water, and in others a hard surface. Bodies are not initially touching. Rotorcraft floor is 12 inches by 50 inches, while beams are 12 inches in height. Impacted body is 100 inches by 12 inches by 50 inches. All rotorcraft models employed identical dimensions.

Figure 4.2.1 Typical Geometry For Rotorcraft Substructure Models

Model employs a rigid sphere and a null material with a linear polynomial equation of state. Bodies are not initially touching. Sphere diameter is .251 meters, and the modeled water is 2.5 diameters on a side, or .627 meters. Water body is 1.25 diameters, or .314 meters in height.

3D RIGID BODY MODEL 2.16
Time = 0

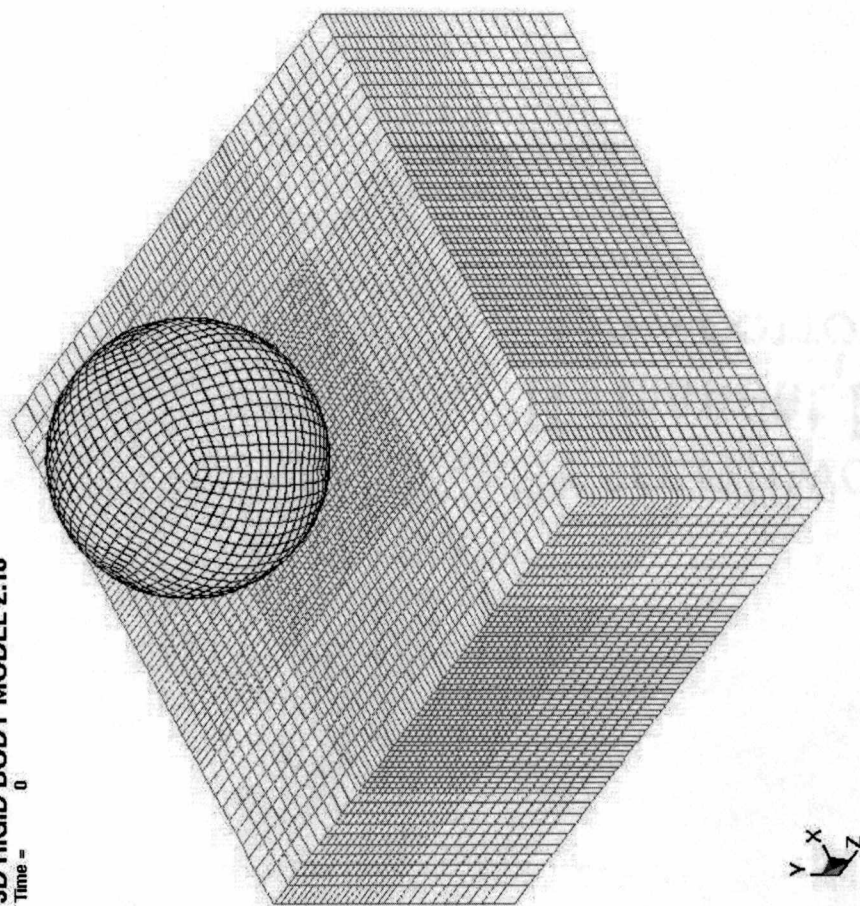


Figure 4.3.1 Model 2.16 at time $t=0.000$ sec

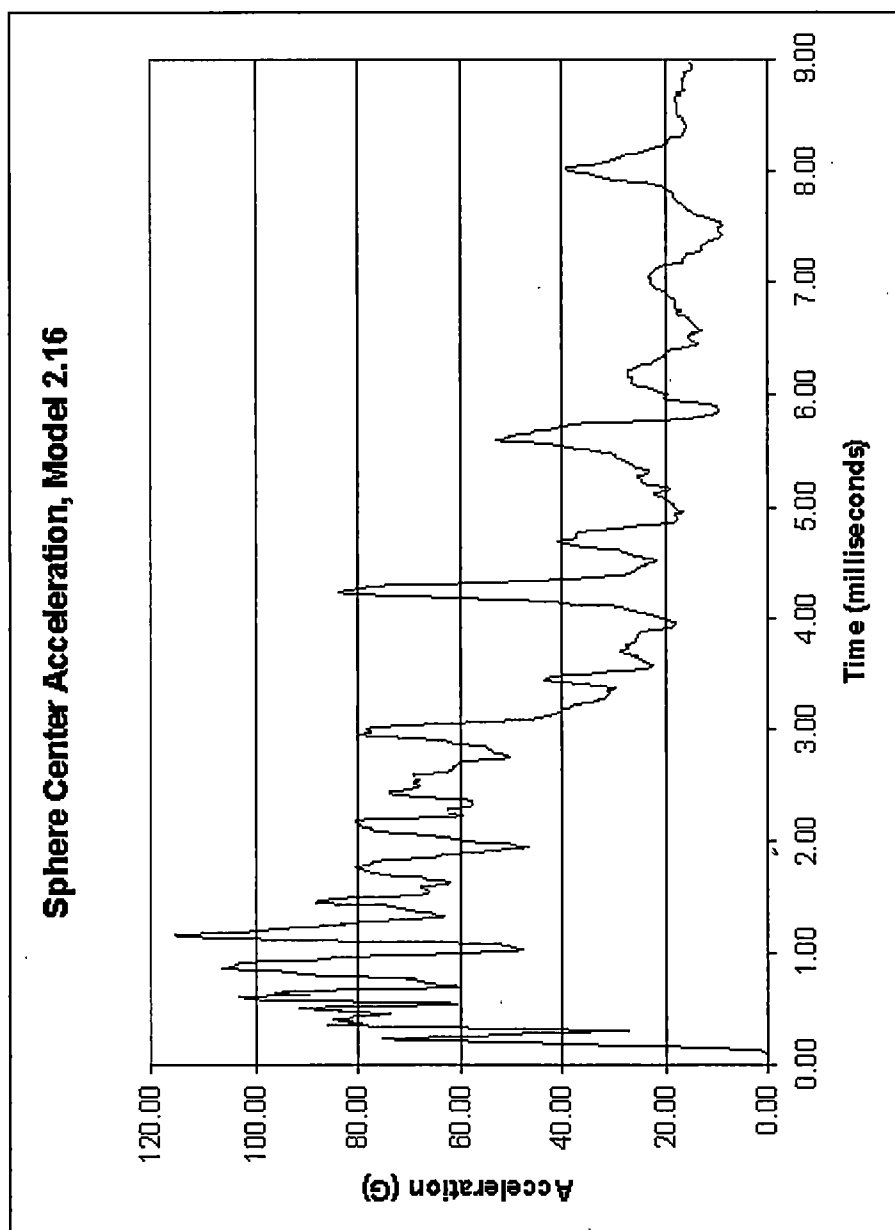


Figure 4.3.2 Sphere Center Acceleration Time History, Model 2.16

3D RIGID BODY MODEL 2.17, LINEAR POLYNO
Time = 0

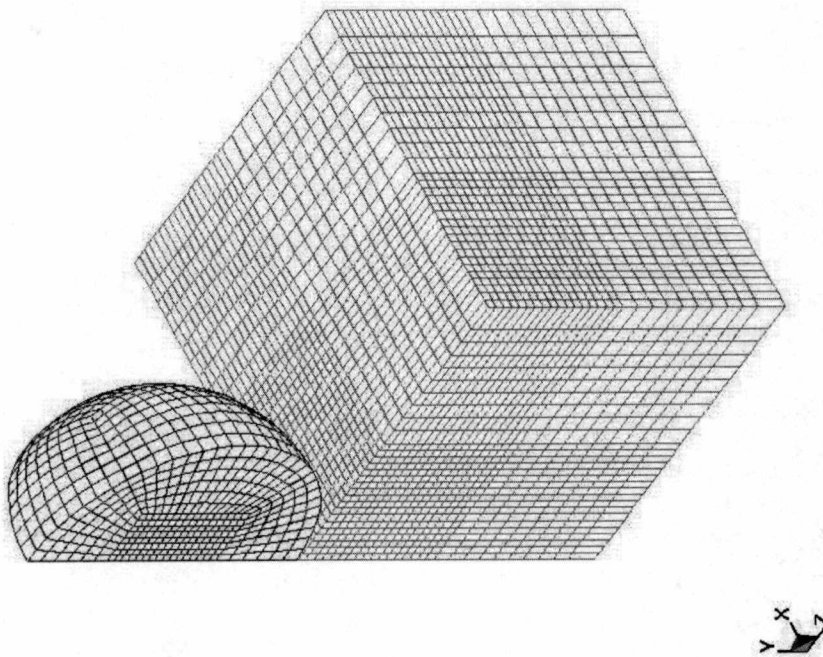


Figure 4.3.3 Model 2.17 at time $t=0.000$ sec

Model employs a rigid sphere and a null material with a linear polynomial equation of state. Bodies are not initially touching. Sphere diameter is .251 meters, and the modeled water is 1.25 diameters on a side, or .314 meters. Water body is 1.25 diameters, or .314 meters in height. Excepting use of 1/4 symmetry, model 2.17 is identical to model 2.16. An ALE formulation is employed for the water material.

Note similarity to figure 4.3.2.
 Since the only difference is the
 use of 1/4 symmetry, this
 validates the use of symmetry.

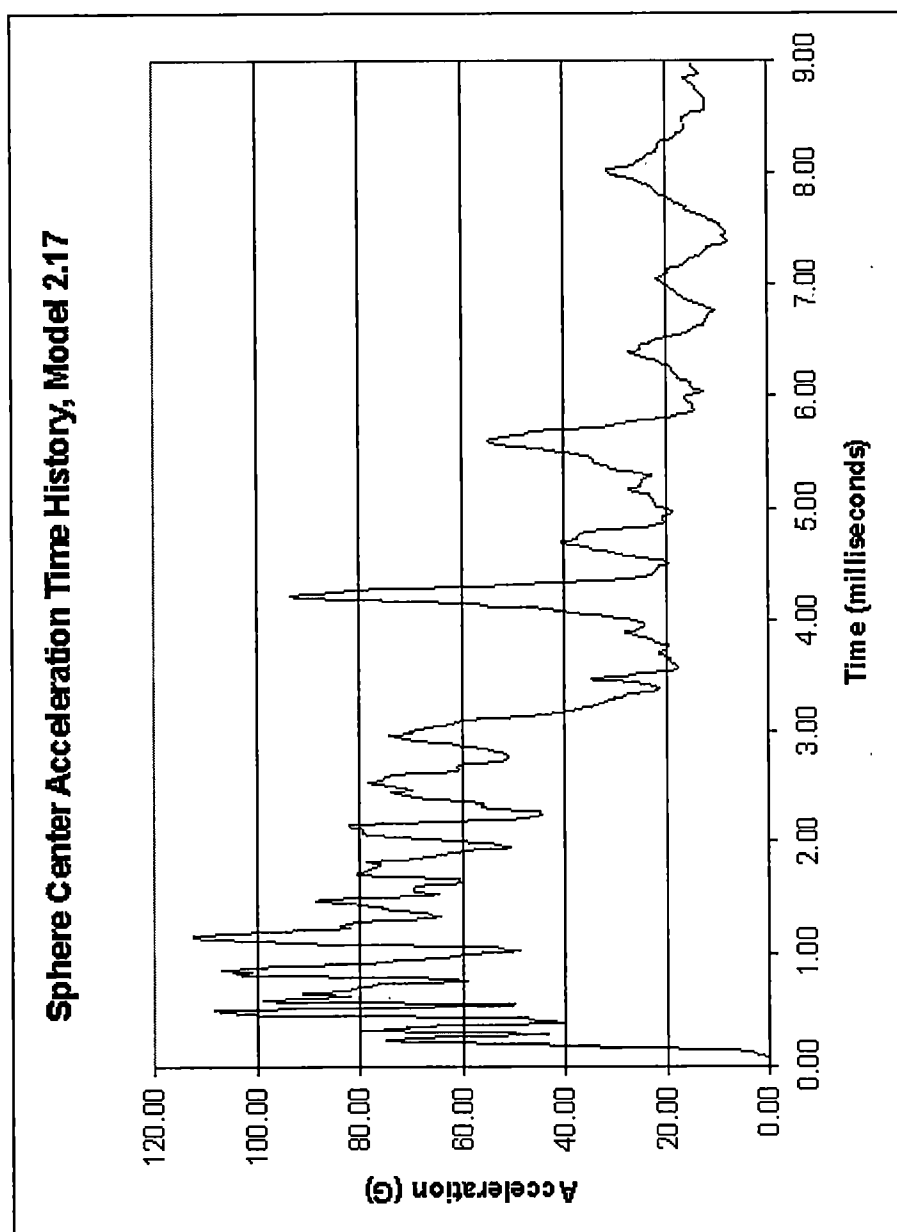


Figure 4.3.4 Sphere Center Acceleration Time History, Model 2.17

Note the minimal effect the eleven point centered running average has. Peaks are only minimally affected.

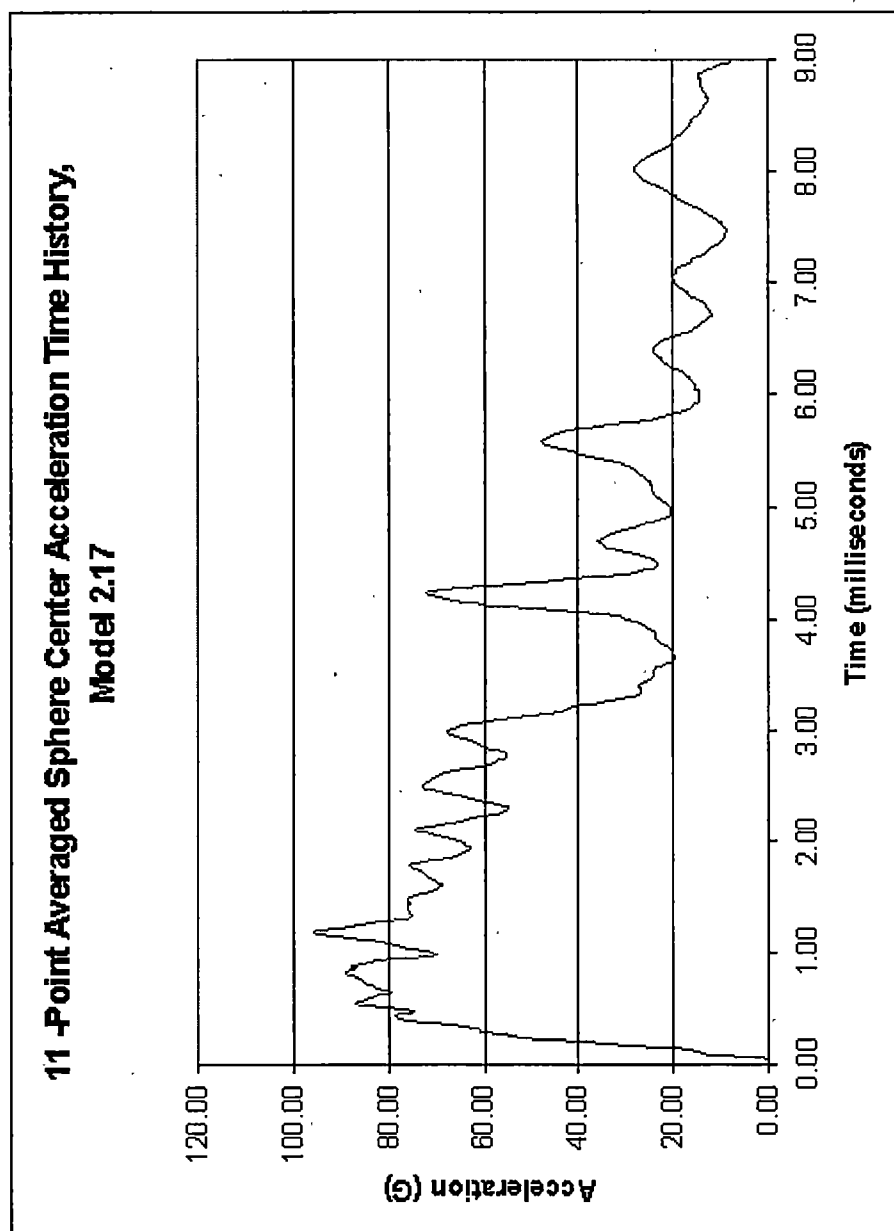


Figure 4.3.5 11-Point Centered Running Average of Sphere Center Acceleration Time History, Model 2.17

Includes a plot of their experimental data, as well as the data from their FEA model. Their model employed a linear polynomial EOS, with a purely Lagrangian formulation, within MSC/Dytran. Note that both were filtered.

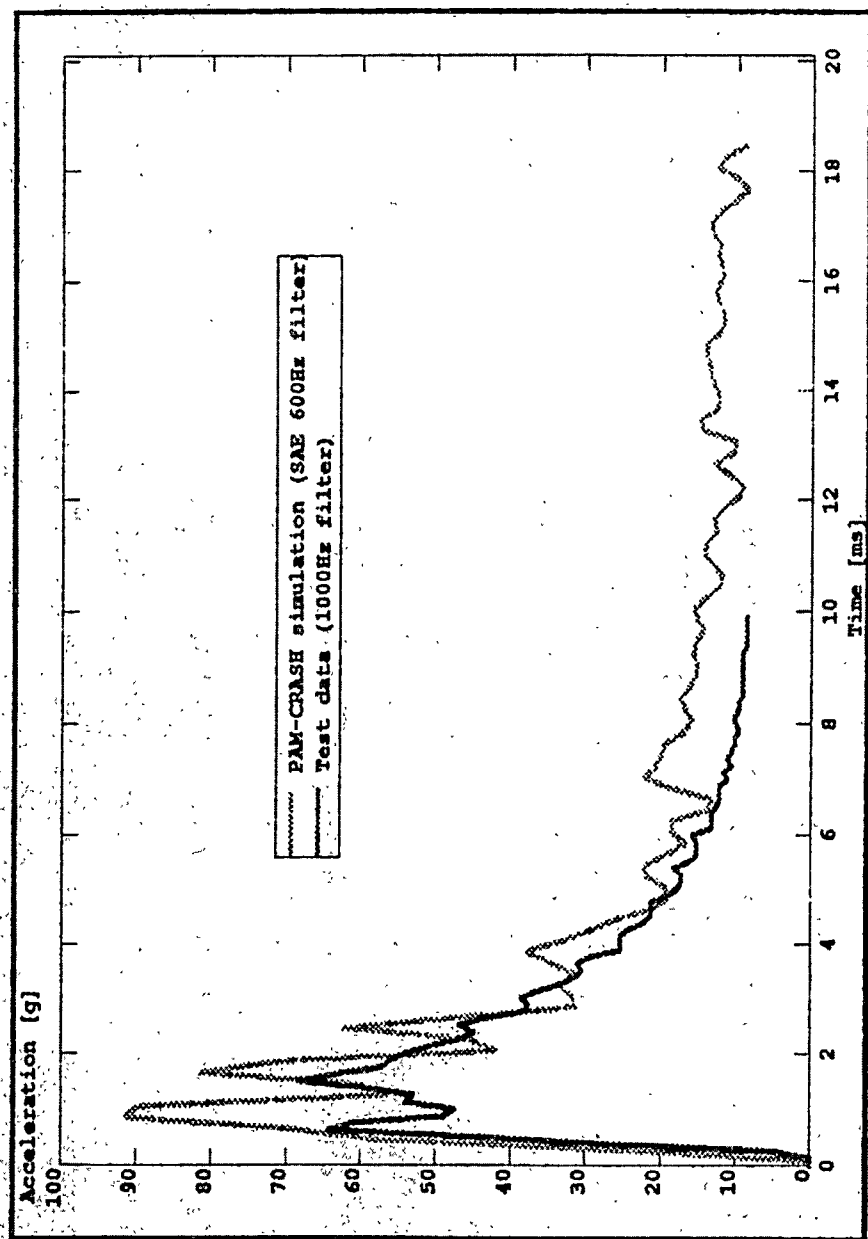


Figure 4.3.6 Experimental Sphere Center Acceleration Time History, From Pentecôte and Kindervater [25]

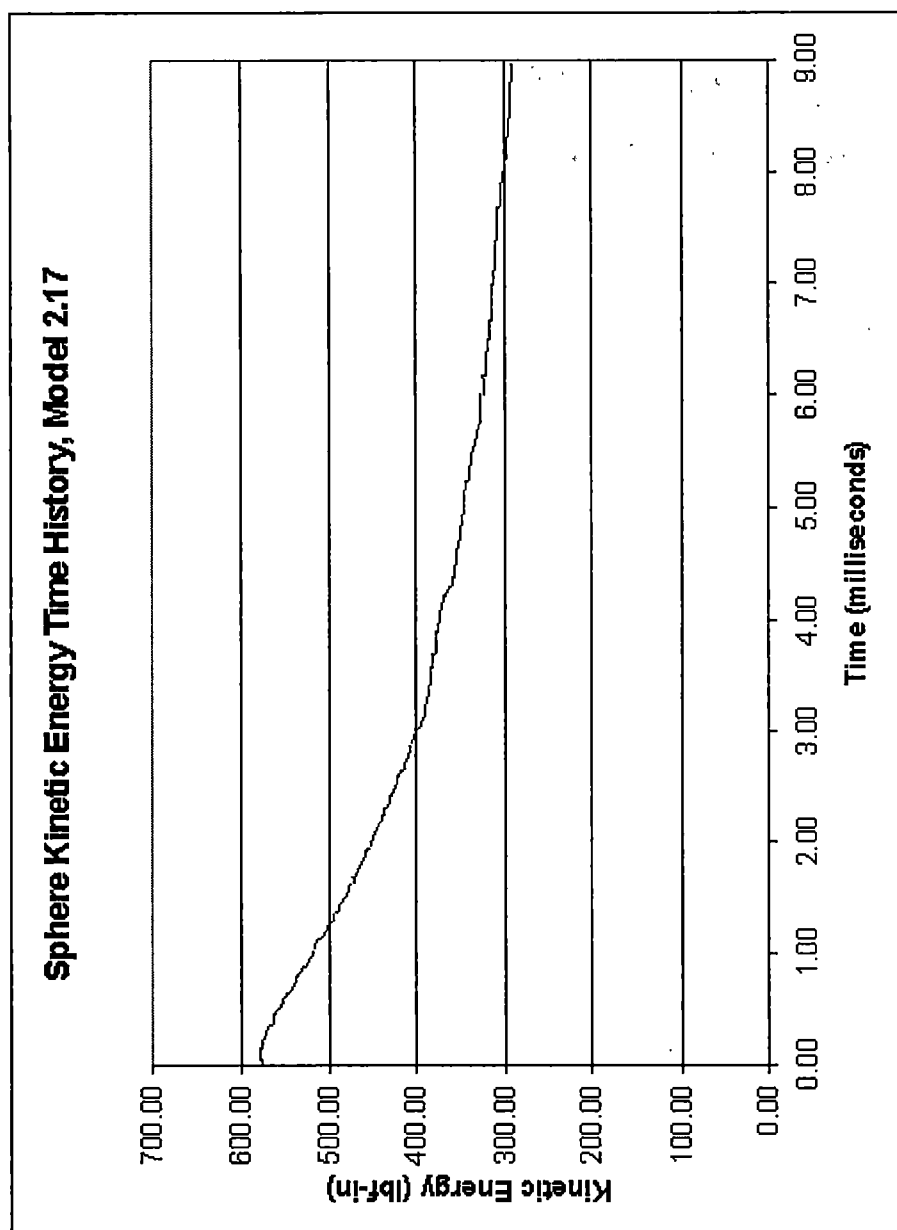


Figure 4.3.7 Sphere Kinetic Energy Time History, Model 2.17

3D RIGID BODY MODEL 2.18, GRUNEISEN EOS
Time = 0

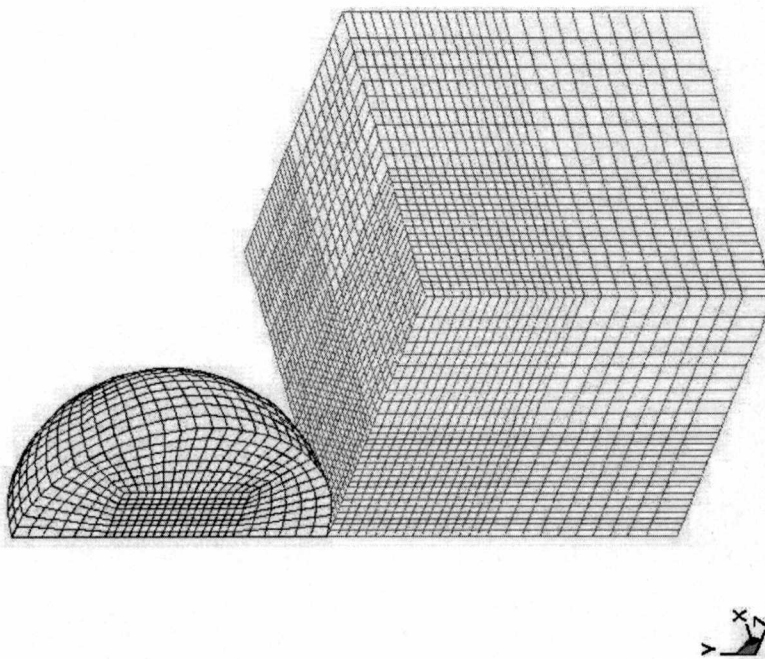


Figure 4.3.8 Model 2.18 at time $t=0.000$ sec

Model employs a rigid sphere and a null material with a Gruneisen equation of state. Bodies are not initially touching. Sphere diameter is .251 meters, and the modeled water is 1.25 diameters on a side, or .314 meters. Water body is 1.25 diameters, or .314 meters in height. Excepting use of the Gruneisen EOS, model 2.18 is identical to model 2.17.

3D RIGID BODY MODEL 2.18, GRUNEISEN EOS
Time = 0.0050199

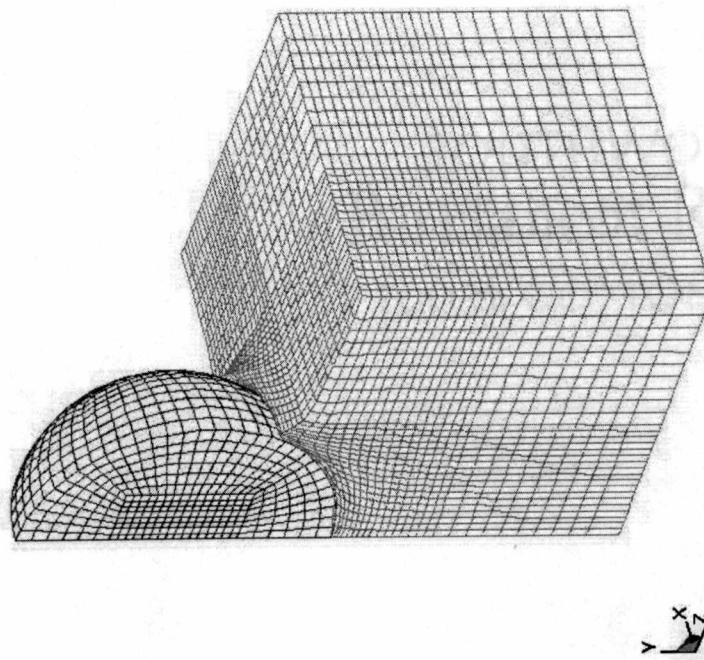


Figure 4.3.9 Model 2.18 at time $t=0.005$ sec

3D RIGID BODY MODEL 2.18, GRUNEISEN EOS
Time = 0.00500003

Note deformation of elements near sphere. This suggests using a purely Lagrangian formulation would be likely to cause errors due to poorly shaped elements.

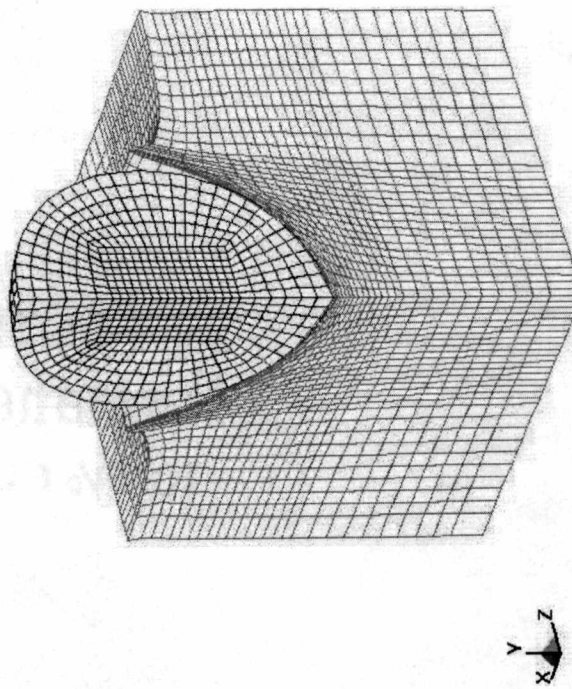


Figure 4.3.10 Model 2.18 at time $t=0.009$ sec

Note similarity to figure 4.3.4. Since the only difference is the use of the Gruneisen EOS, the model is insensitive to EOS selection.

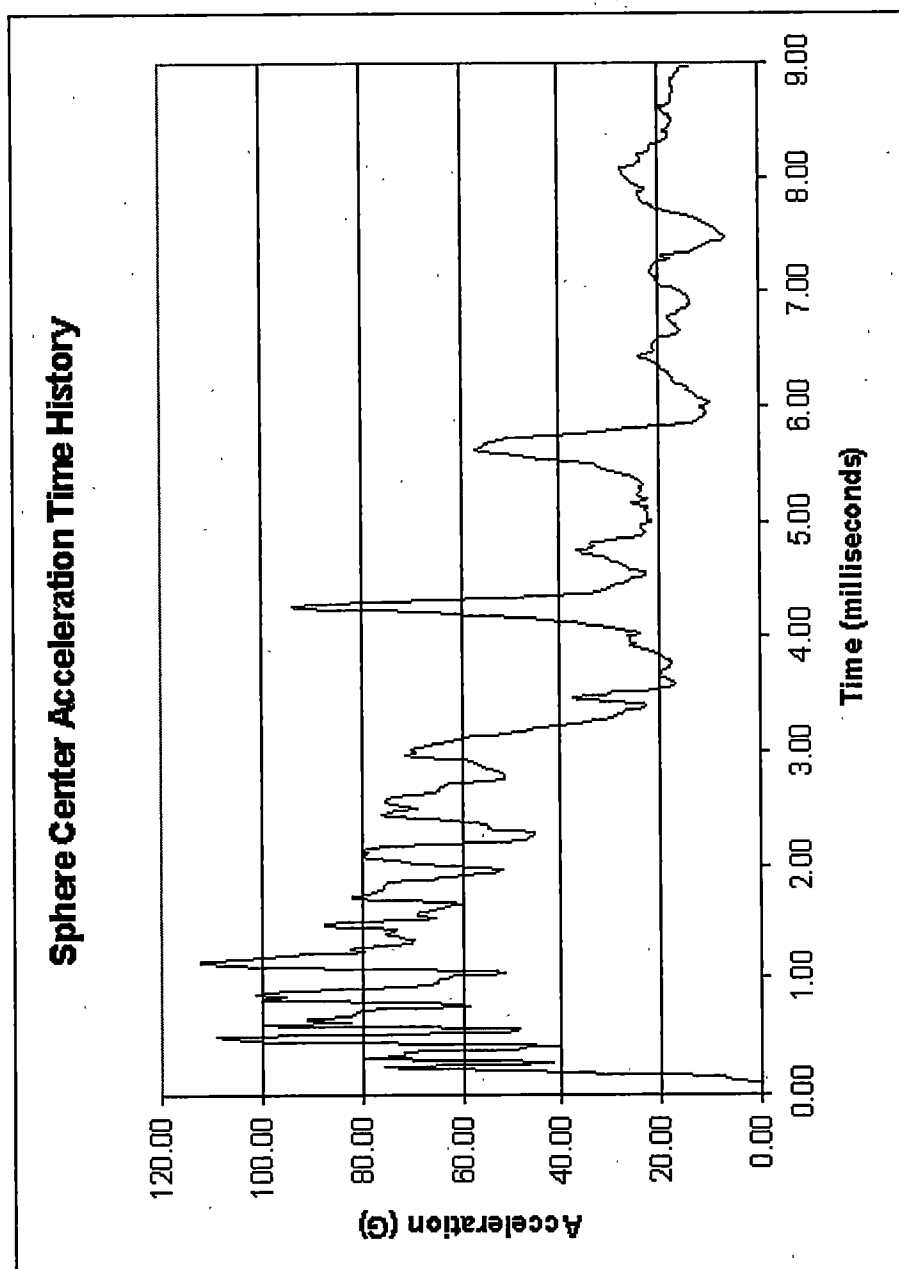


Figure 4.3.11 Sphere Center Acceleration Time History, Model 2.18

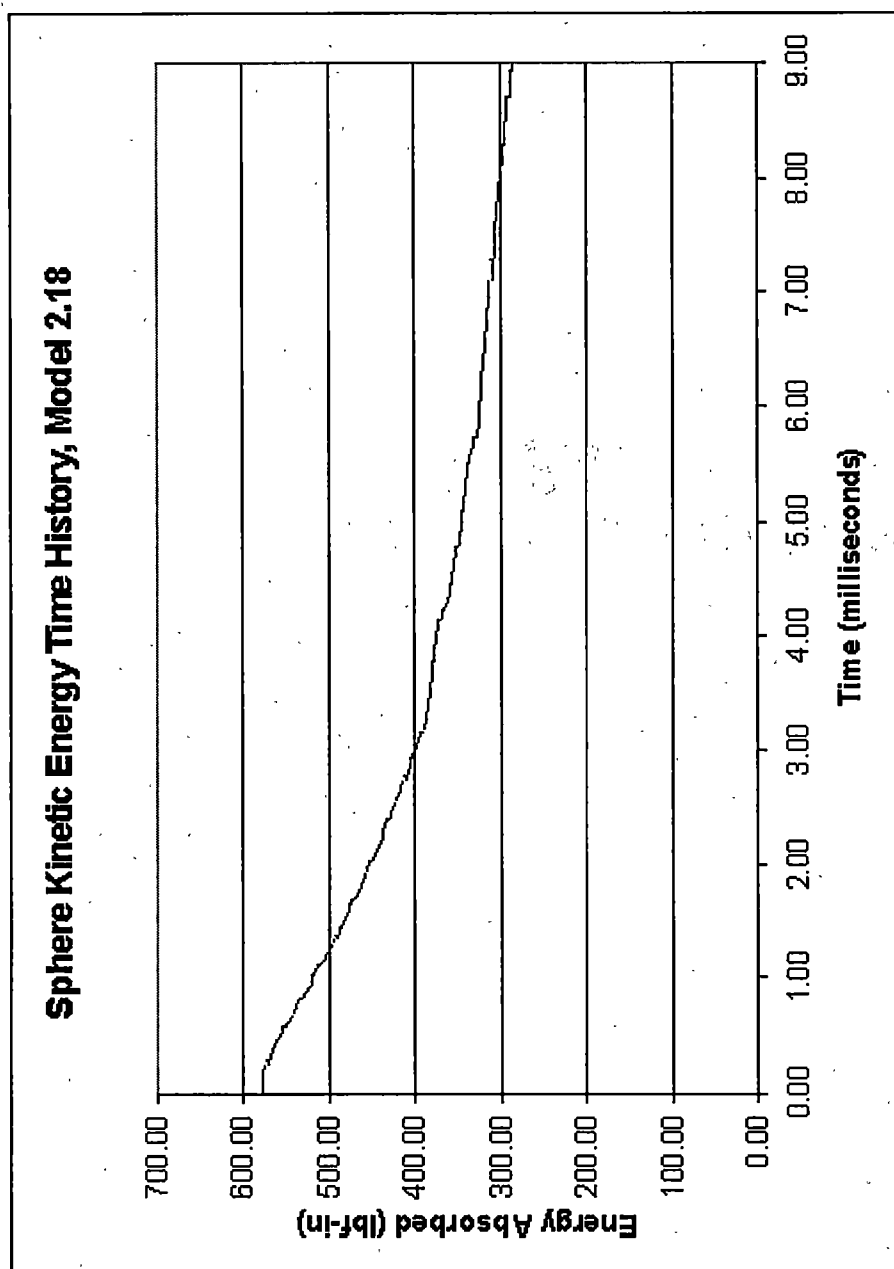


Figure 4.3.12 Sphere Kinetic Energy Time History, Model 2.18

Note peak pressure, and the rapid change compare with following figures.

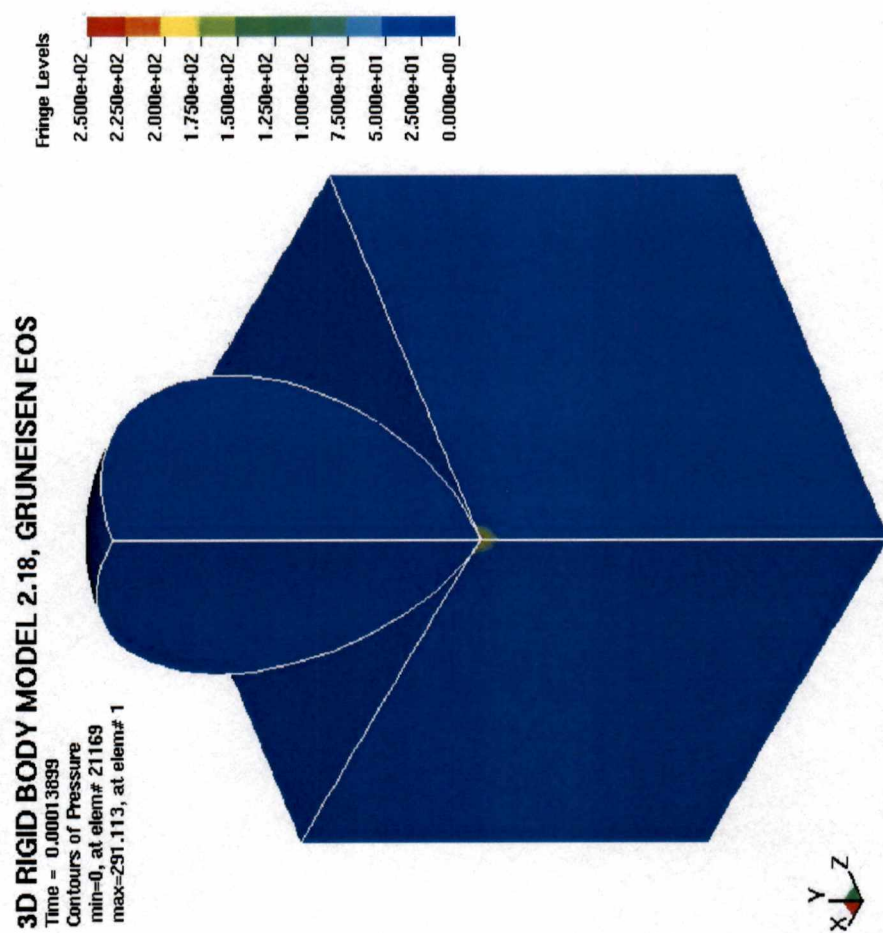
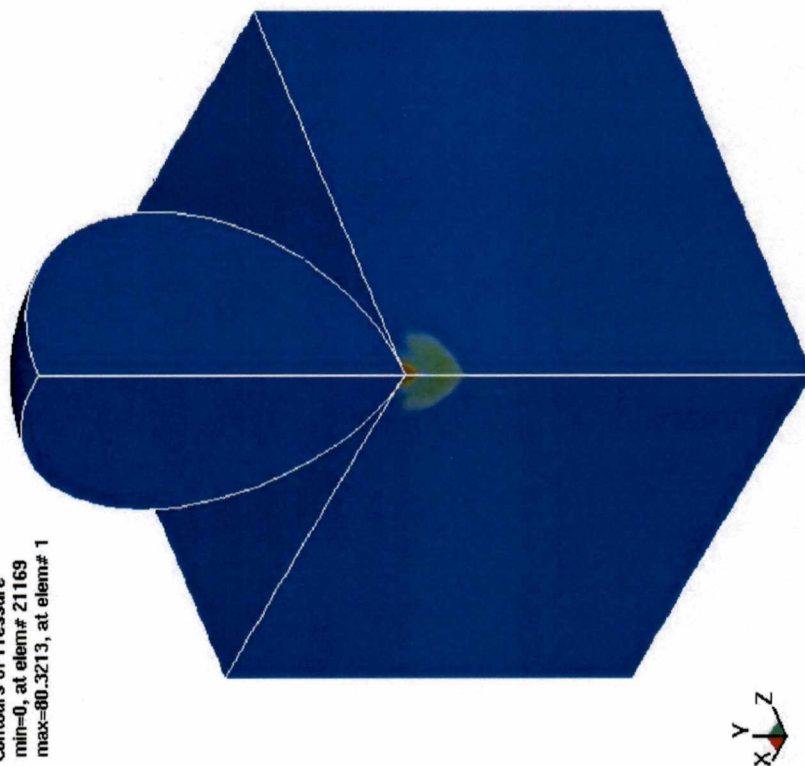
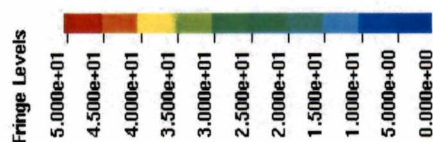


Figure 4.3.13 Pressure Plot at time $t=0.139$ milliseconds, Model 2.18

3D RIGID BODY MODEL 2.18, GRUNEISEN EOS

Time = 0.00015716
 Contours of Pressure
 min=0, at elem# 21169
 max=80.3213, at elem# 1



Compare peak pressure with that in figure 4.3.11, just .002 milliseconds earlier. Note the fringe level change as well.

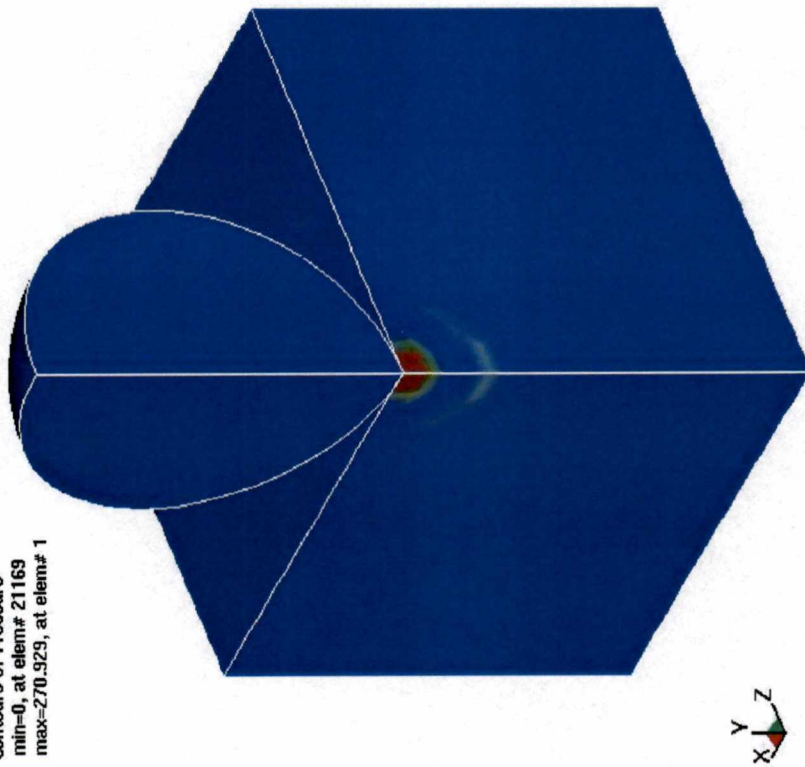
Figure 4.3.14 Pressure Plot at time $t=0.157$ milliseconds, Model 2.18

3D RIGID BODY MODEL 2.18, GRUNEISEN EOS

Time = 0.00017831
Contours of Pressure
min=0, at elem# 21169
max=270.929, at elem# 1

Fringe Levels

5.000e+01
4.500e+01
4.000e+01
3.500e+01
3.000e+01
2.500e+01
2.000e+01
1.500e+01
1.000e+01
5.000e+00
0.000e+00

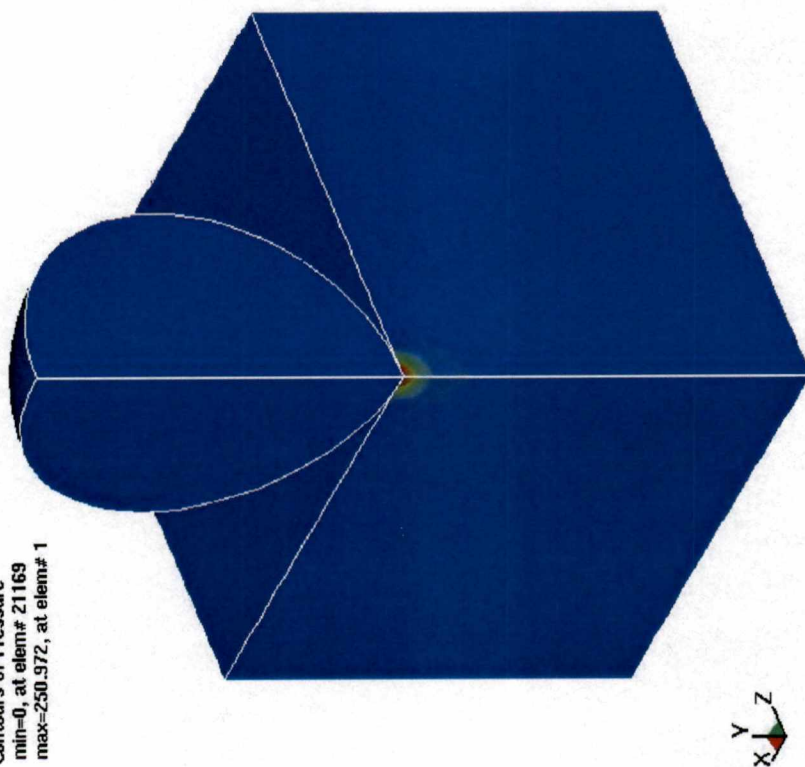
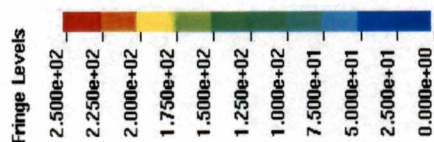


Note the propagation of the pressure wave away from the contact point, and the rapid increase in the peak pressure compared with figure 4.3.12, just .02 milliseconds earlier. The lower pressure wave visible has greatly dissipated, and a new pressure wave is forming behind it.

Figure 4.3.15 Pressure Plot at time t=0.178 milliseconds, Model 2.18

3D RIGID BODY MODEL 2.18, GRUNEISEN EOS

Time = 0.00019937
 Contours of Pressure
 min=0, at elem# 21169
 max=250.972, at elem# 1



Again, note the rapidly swinging peak pressure compared with preceding figures. Note the fringe level changes as well.

Figure 4.3.16 Pressure Plot at time $t=0.199$ milliseconds, Model 2.18

Model is identical to model 2.17, except for the use of a purely Lagrangian formulation.

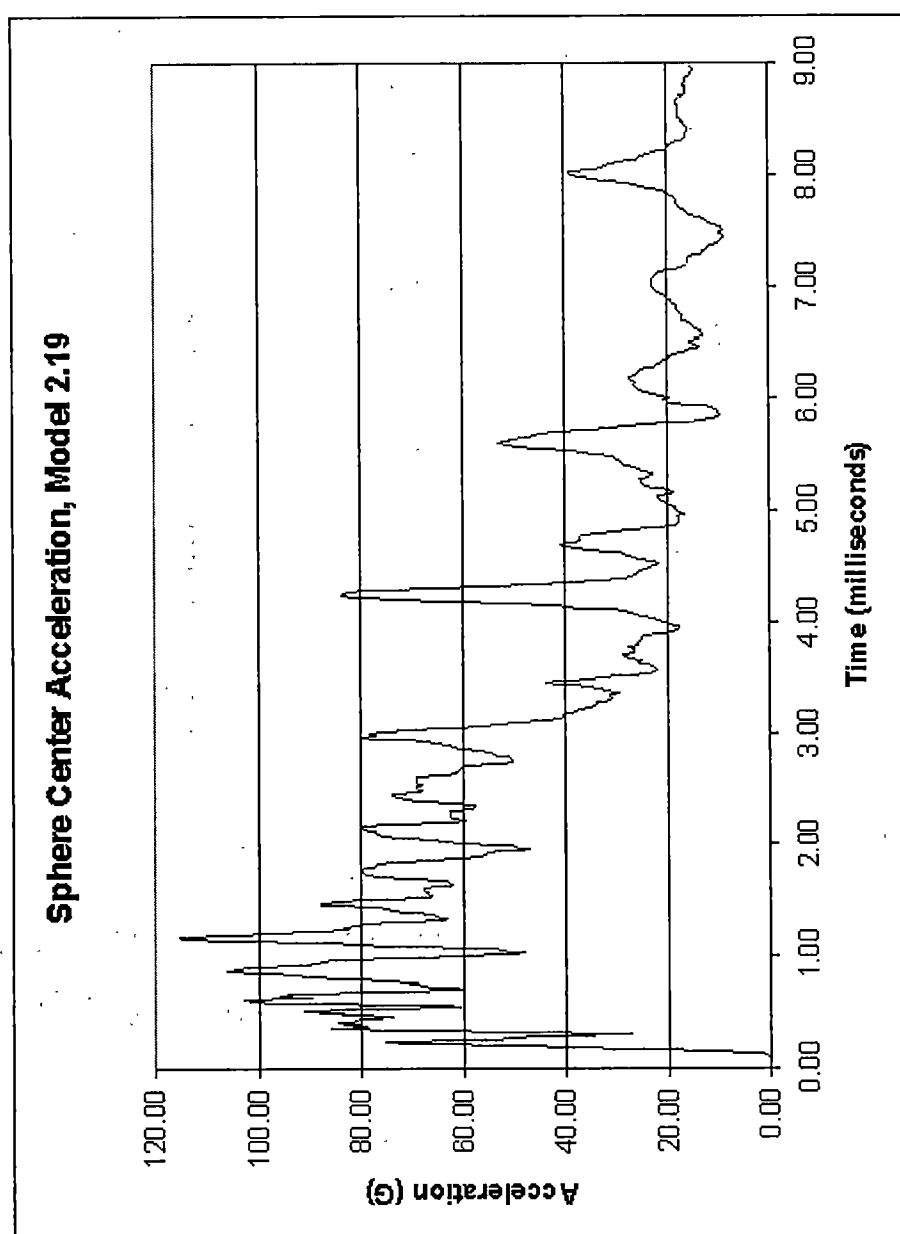


Figure 4.3.17 Sphere Center Acceleration Time History, Model 2.19

Model is identical to model 2.17, except for the use of a purely Eulerian formulation.

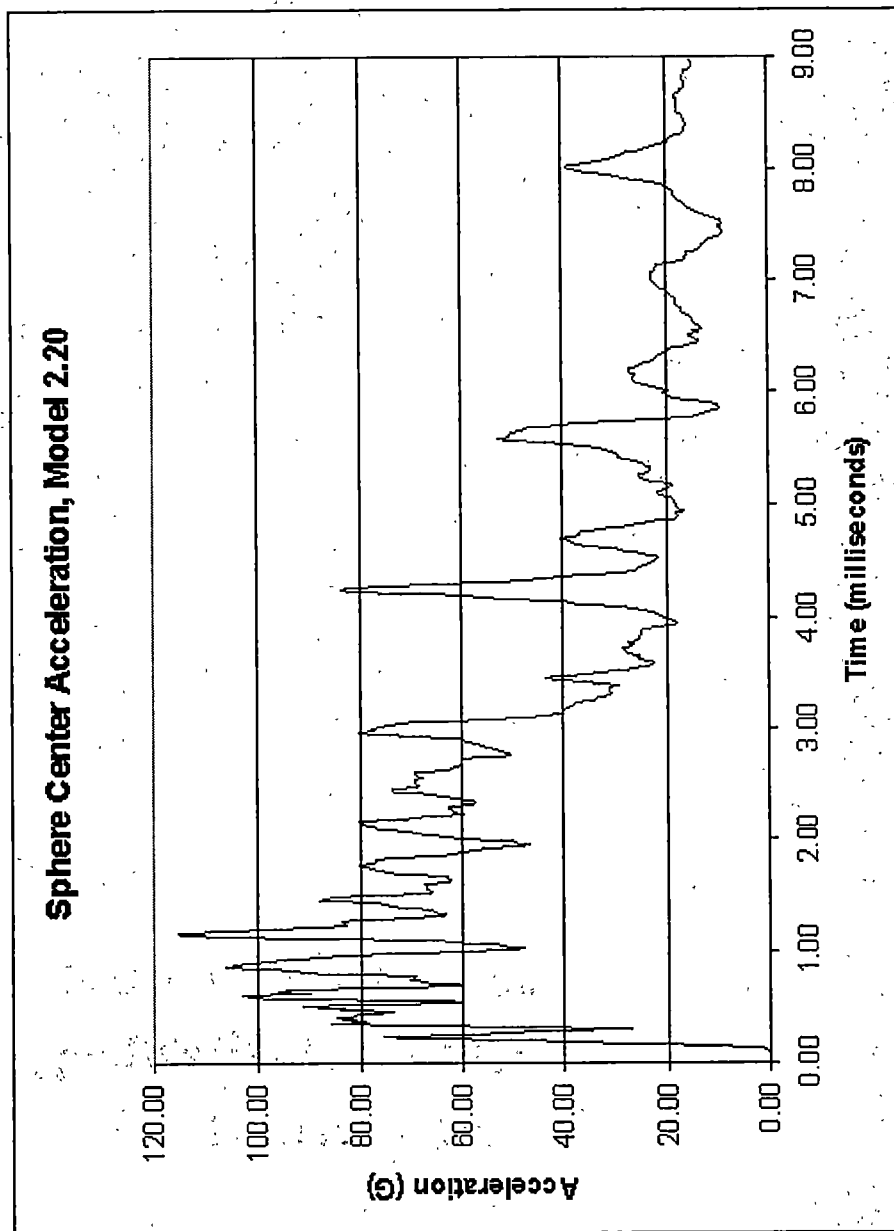
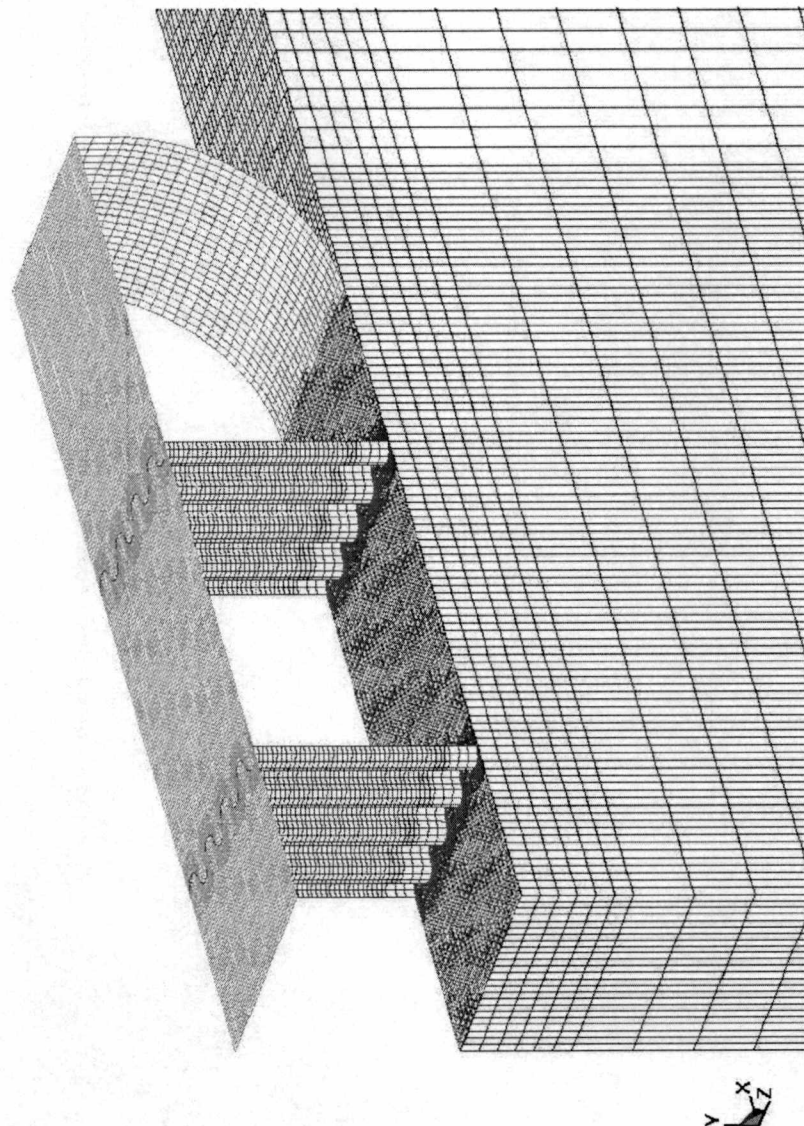


Figure 4.3.18 Sphere Center Acceleration Time History, Model 2.20

3D MODEL 3.16, PLASTIC FAILURE AL
Time = 0



Rotorcraft substructure consists of two sine wave web beams, the rotorcraft floor, and the skin. Impacted body is rigid material representing a hard surface. Bodies are not initially touching. Rotorcraft beams and skin employ a linear elastic, linear plastic, maximum strain failure material representing 2024-T4 aluminum alloy. Rotorcraft floor is rigid. Initiator located near bottom.

Figure 4.4.1.1 Model 3.16 at time $t=0.000$ sec

Note failure beginning along the bottom of the beams.

3D MODEL 3.16, PLASTIC FAILURE AL
Time = 0.0024496

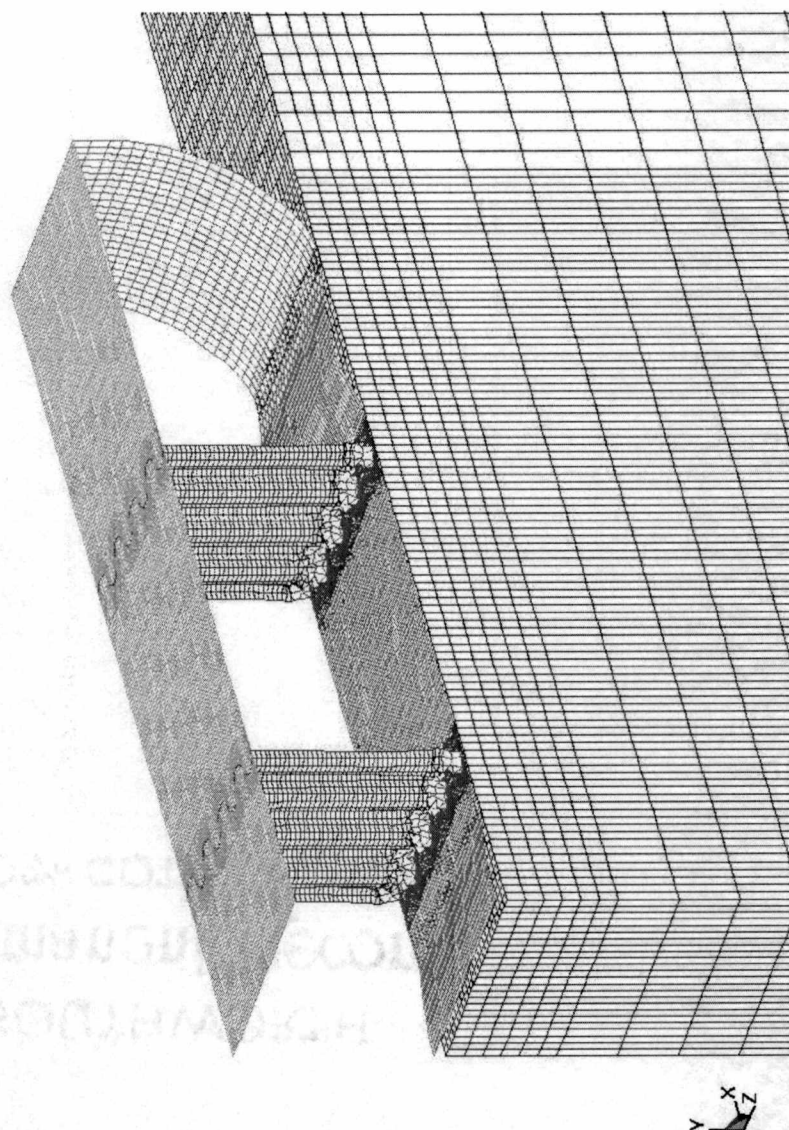


Figure 4.4.1.2 Model 3.16 at time $t=0.0025$ sec

3D MODEL 3.16, PLASTIC FAILURE AL
Time = 0.0050002

Failure has propagated. Note crushing is confined to a small area, and global buckling has been avoided.

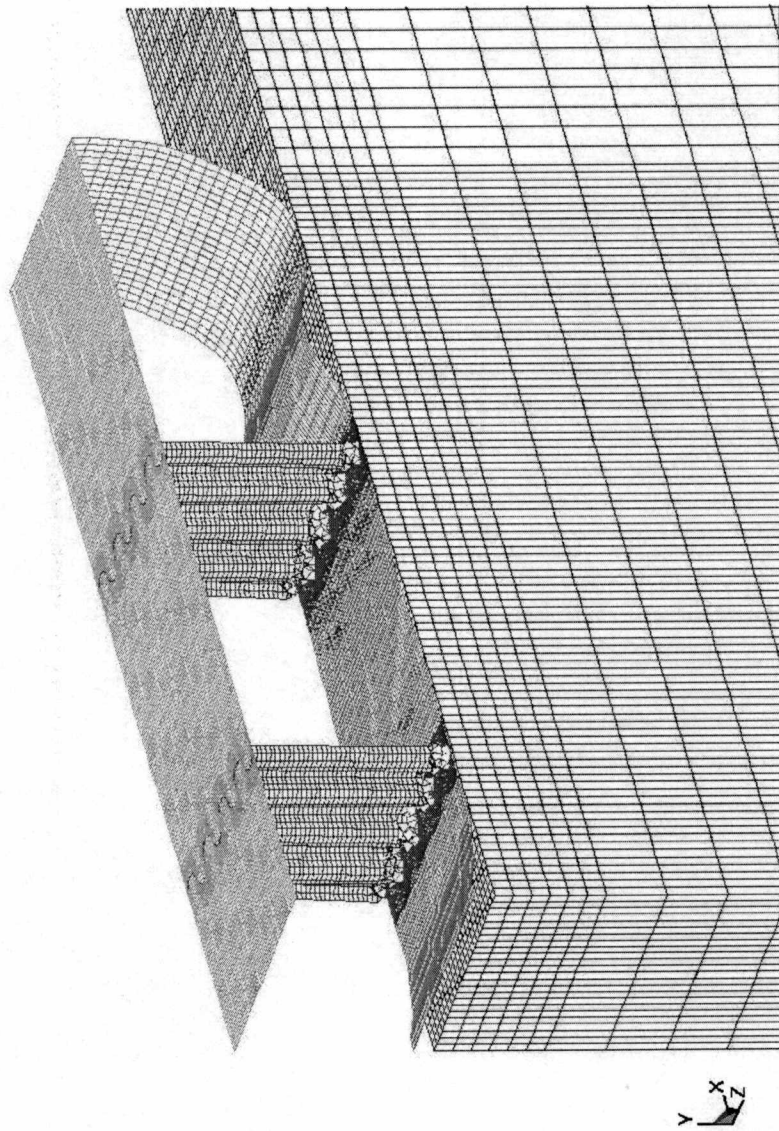


Figure 4.4.1.3 Model 3.16 at time $t=0.005$ sec

Note early peak, well above the optimal 20G. Also note the sustained acceleration at later times is well below 20G.

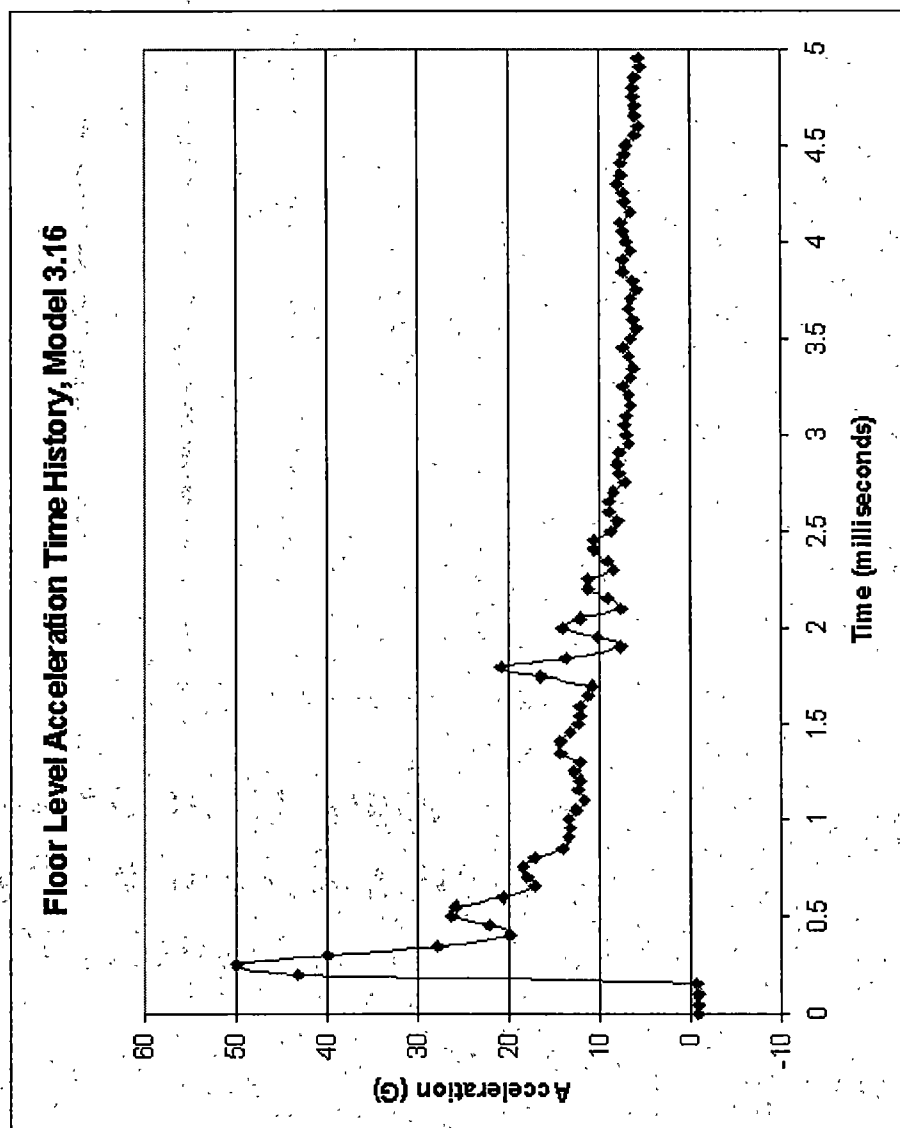


Figure 4.4.1.4 Floor Level Acceleration Time History, Model 3.16

Peak value of 7592 lbf-in represents approximately 14.1% of the total of 53477 lbf-in of kinetic energy in the structure at impact.

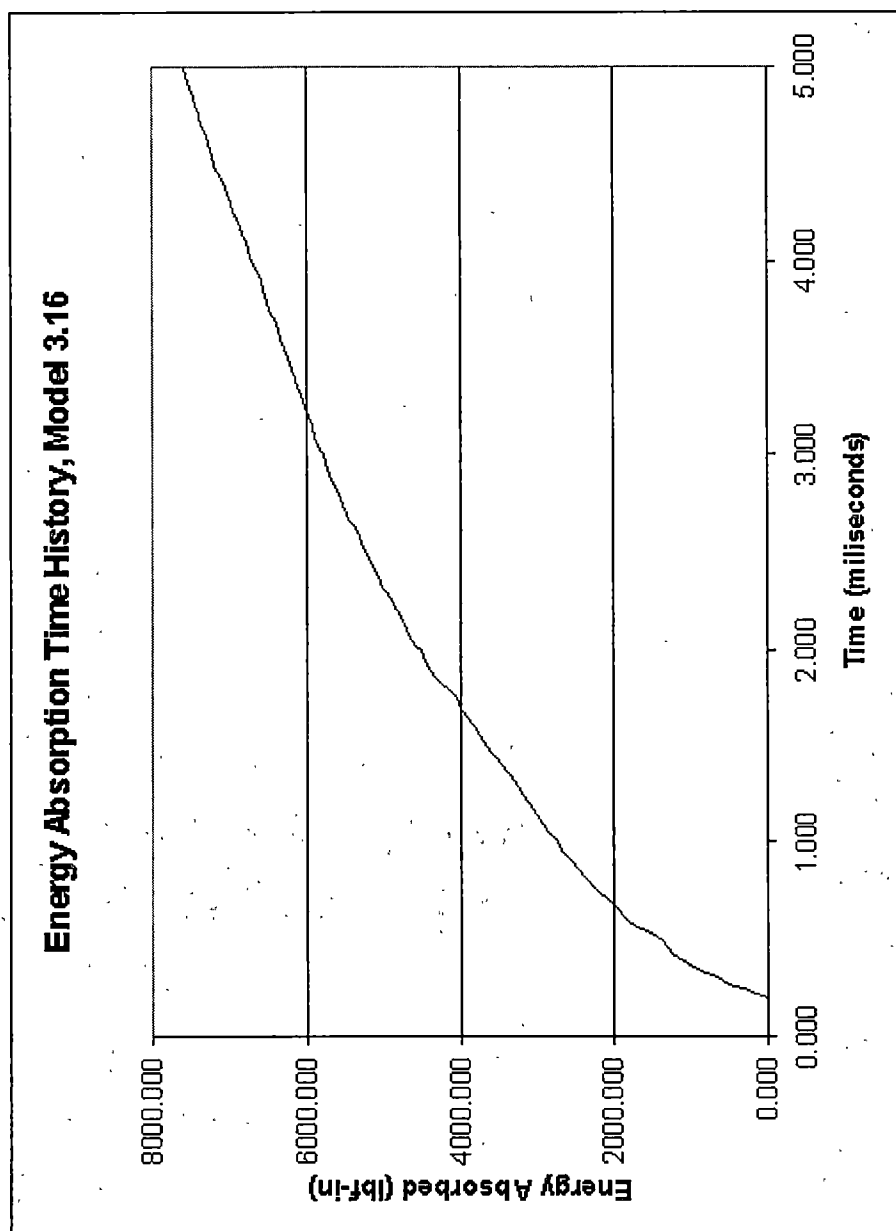
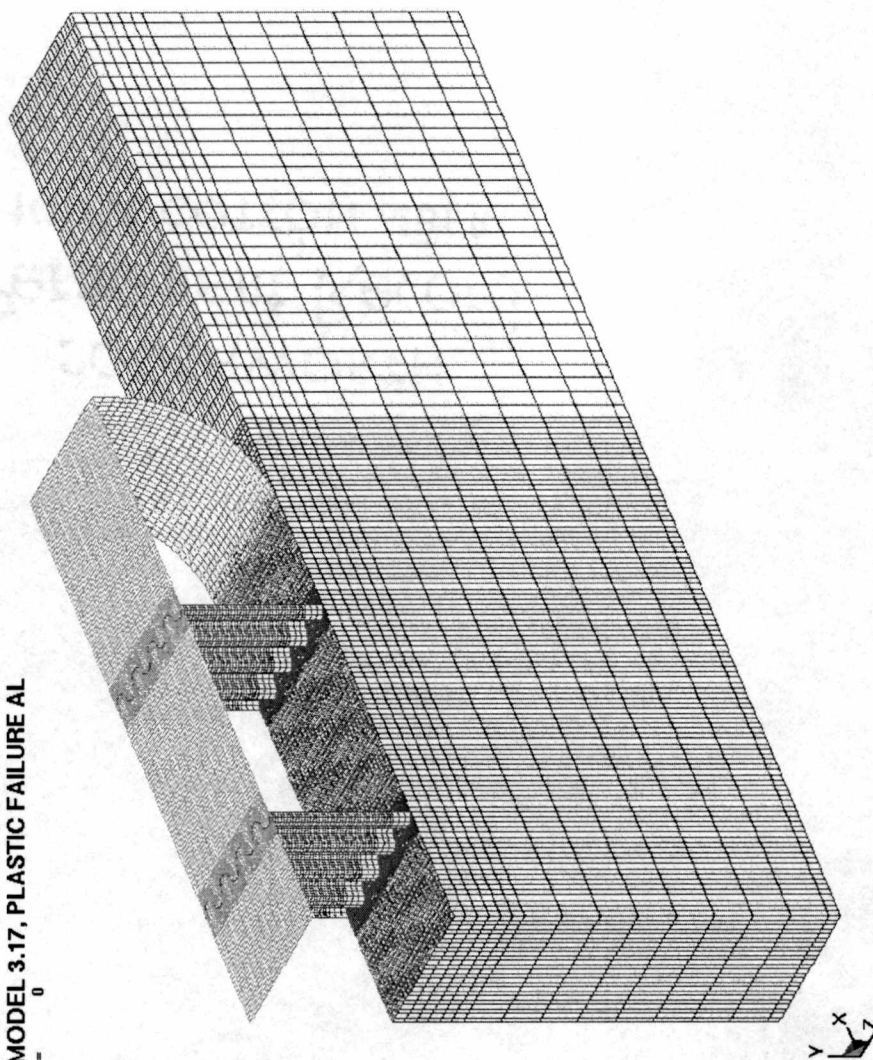


Figure 4.4.1.5 Energy Absorption Time History, Model 3.16

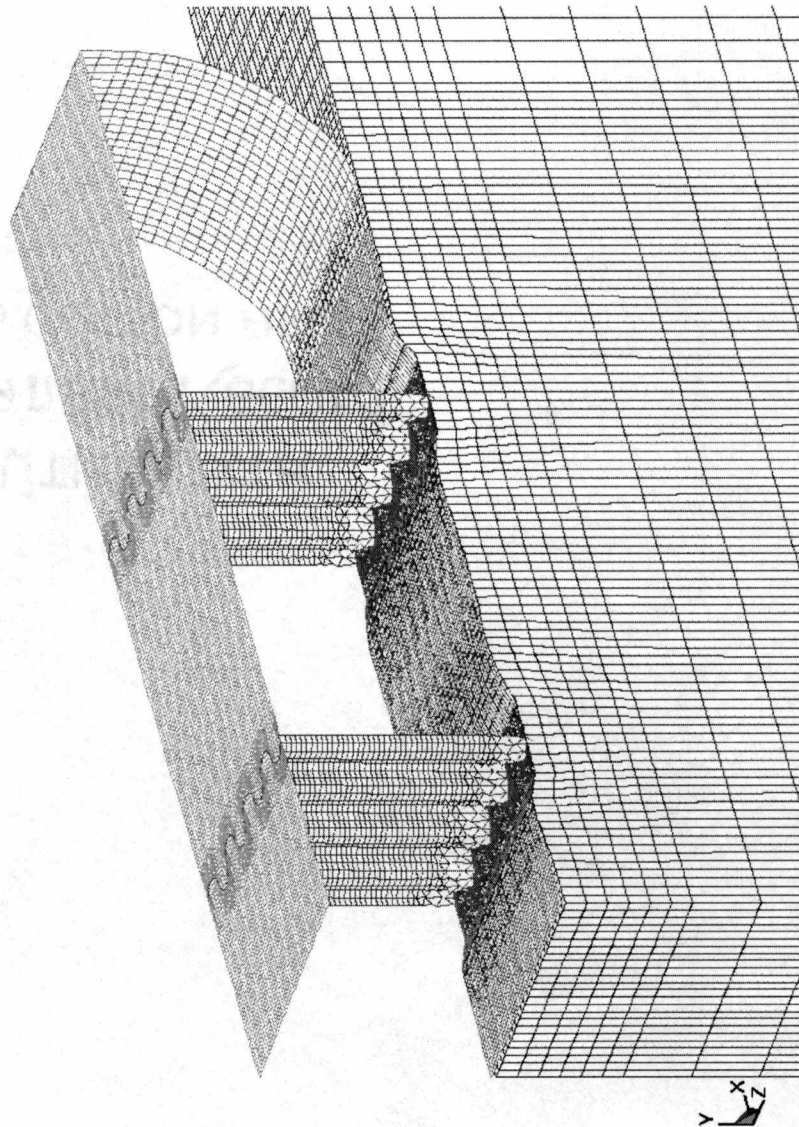
3D MODEL 3.17, PLASTIC FAILURE AL
Time = 0



Rotorcraft substructure consists of two sine wave web beams, the rotorcraft floor, and the skin. Impacted body is a null material with a linear polynomial EOS representing water. Bodies are not initially touching. Rotorcraft beams and skin employ a linear elastic, linear plastic, maximum strain failure material representing 2024-T4 aluminum alloy. Rotorcraft floor is rigid. Initiator located near bottom. Except for impacted body material, model 3.17 is identical to model 3.16.

Figure 4.4.1.6 Model 3.17 at time $t=0.000$ sec

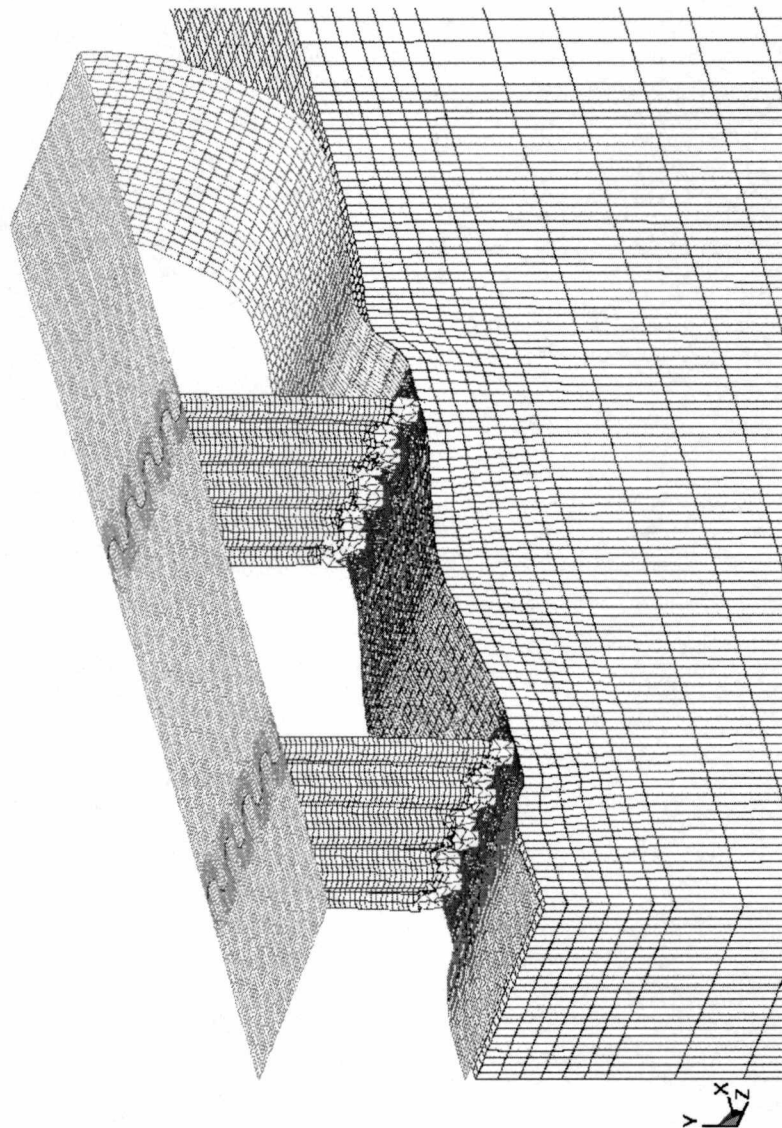
3D MODEL 3.17, PLASTIC FAILURE AL
Time = 0.0022396



Note the lack of deformation near the center of the skin between the beams. Since the skin has not deformed, applied pressure must be very small, and so the skin behavior cannot have significant effect on the floor level accelerations until after this time. The beams alone are responsible for attenuating the impact acceleration, and their footings are applying force to the water.

Figure 4.4.1.7 Model 3.17 at time $t=0.0023$ sec

3D MODEL 3.17, PLASTIC FAILURE AL
Time = 0.0050001



In comparison to Figure 4.4.1.7 the skin between the beams is deformed. Full contact pressure has been developed, and the skin has not ruptured. At these later times, both the skin and beam footings are applying force to the water, and so both the skin and beams can have significant effect on floor level accelerations.

Figure 4.4.1.8 Model 3.17 at Time $t=0.005$ sec

Compared with Figure 4.4.1.4,
note the lower peak
accelerations, and the higher
sustained acceleration levels.

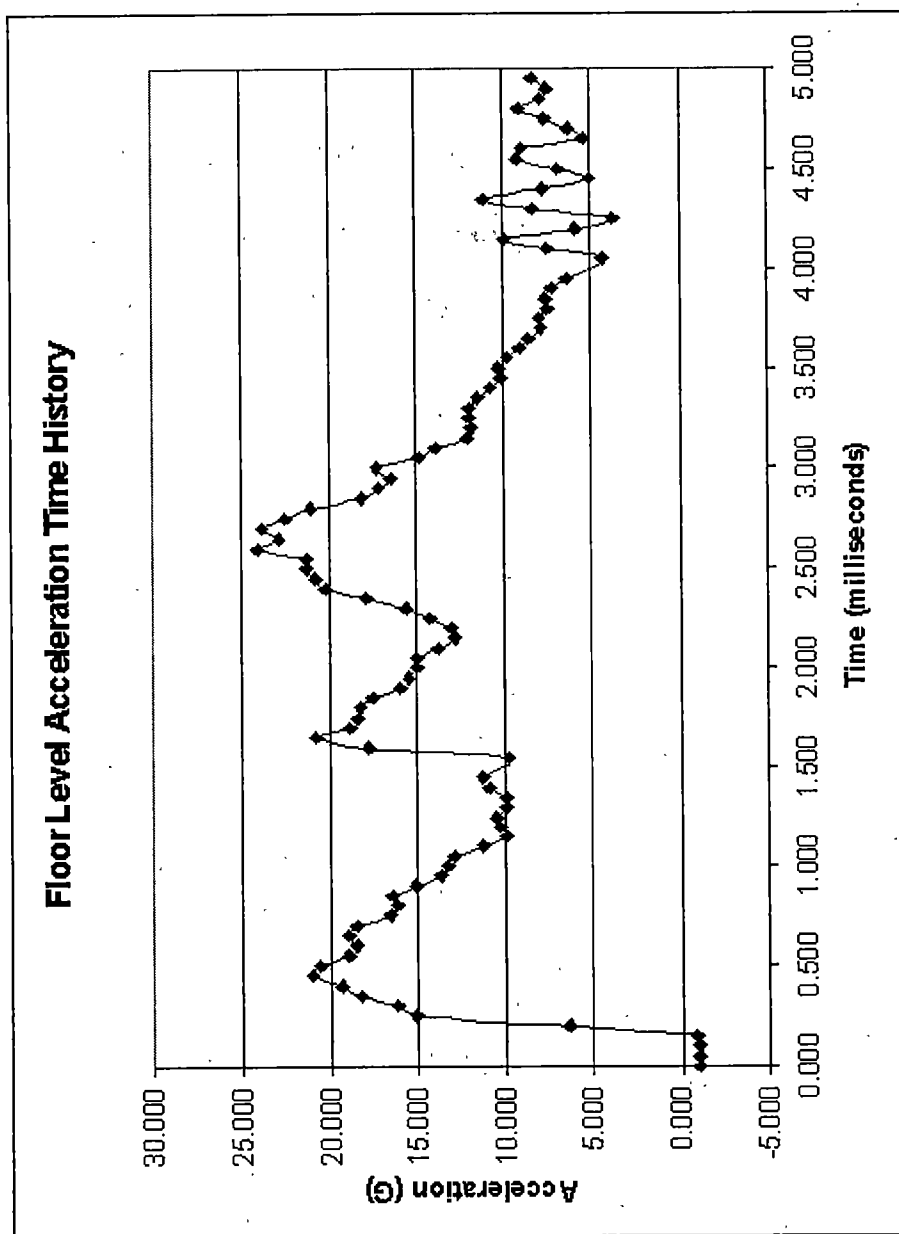


Figure 4.4.1.9 Floor Level Acceleration Time History, Model 3.17

Peak value of 10797 lbf-in represents approximately 20.1% of the total of 53477 lbf-in of kinetic energy in the structure at impact. Unsurprisingly, the higher sustained accelerations permit better energy absorption than model 3.16.

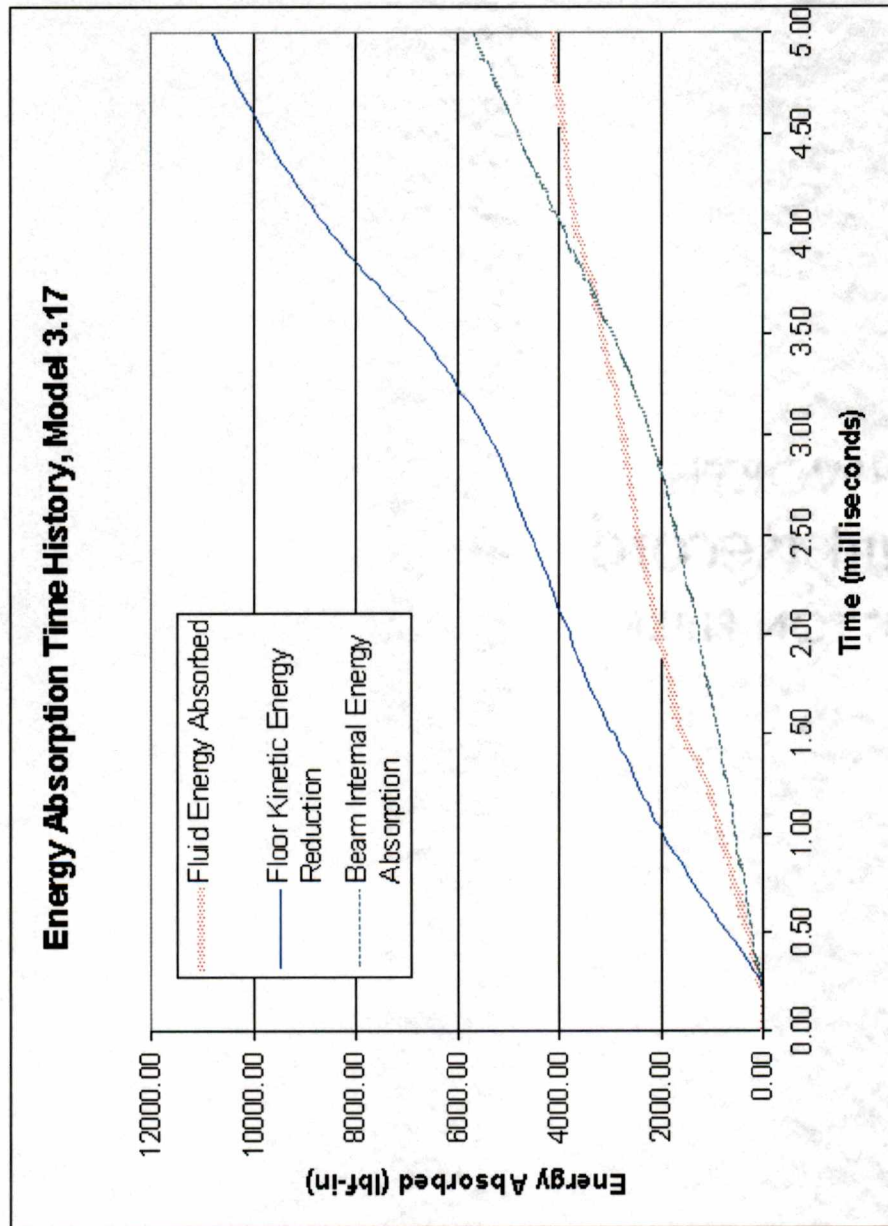


Figure 4.4.1.10 Energy Absorption Time History, Model 3.17

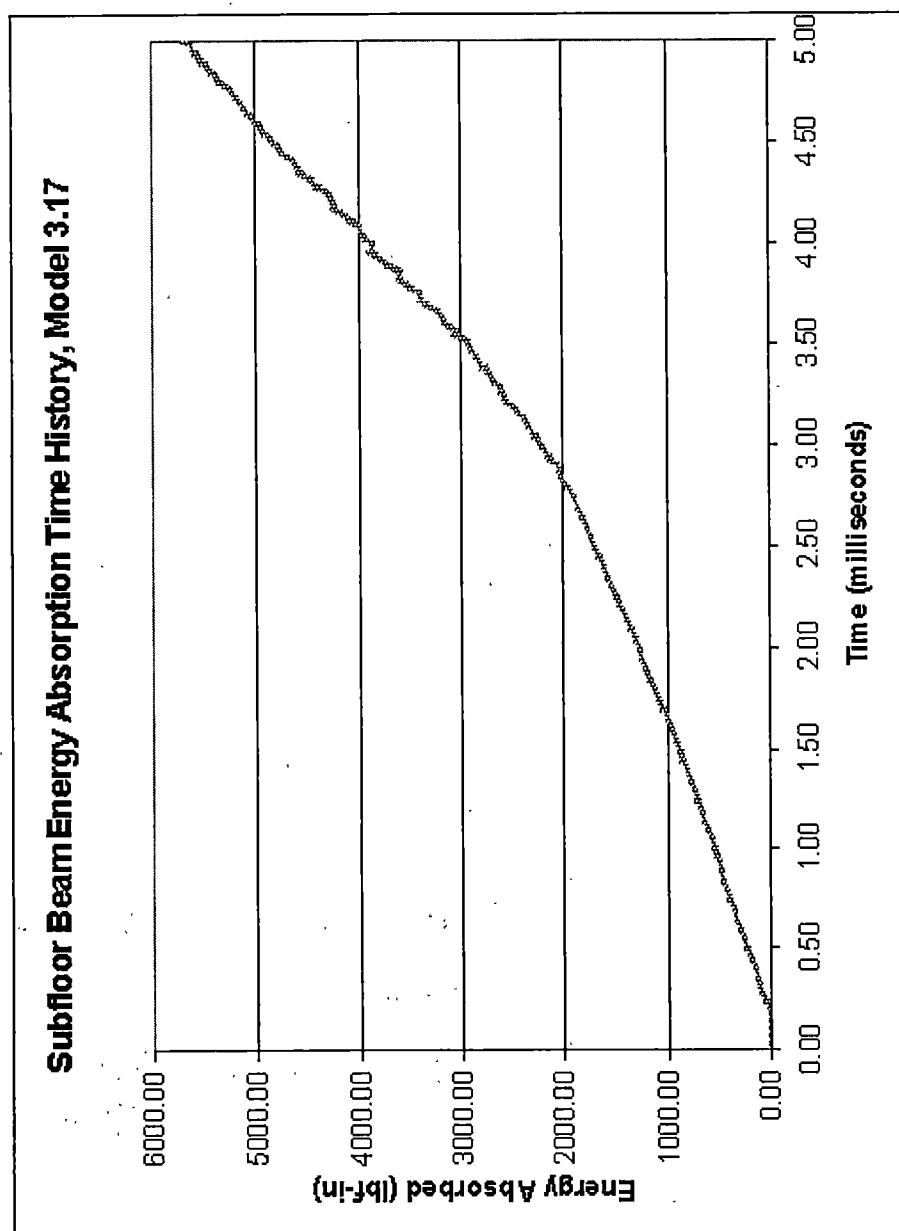


Figure 4.4.1.11 Subfloor Beam Energy Absorption Time History, Model 3.17

3D MODEL 3.17, PLASTIC FAILURE AL

Time = 0.00029952
Contours of Pressure
max ip1, value
min=-1824.59, at elem# 12286
max=13547.2, at elem# 13423

Note two pressure waves located under the beam. Each began just under the beam and has propagated away from the rotorcraft structure.

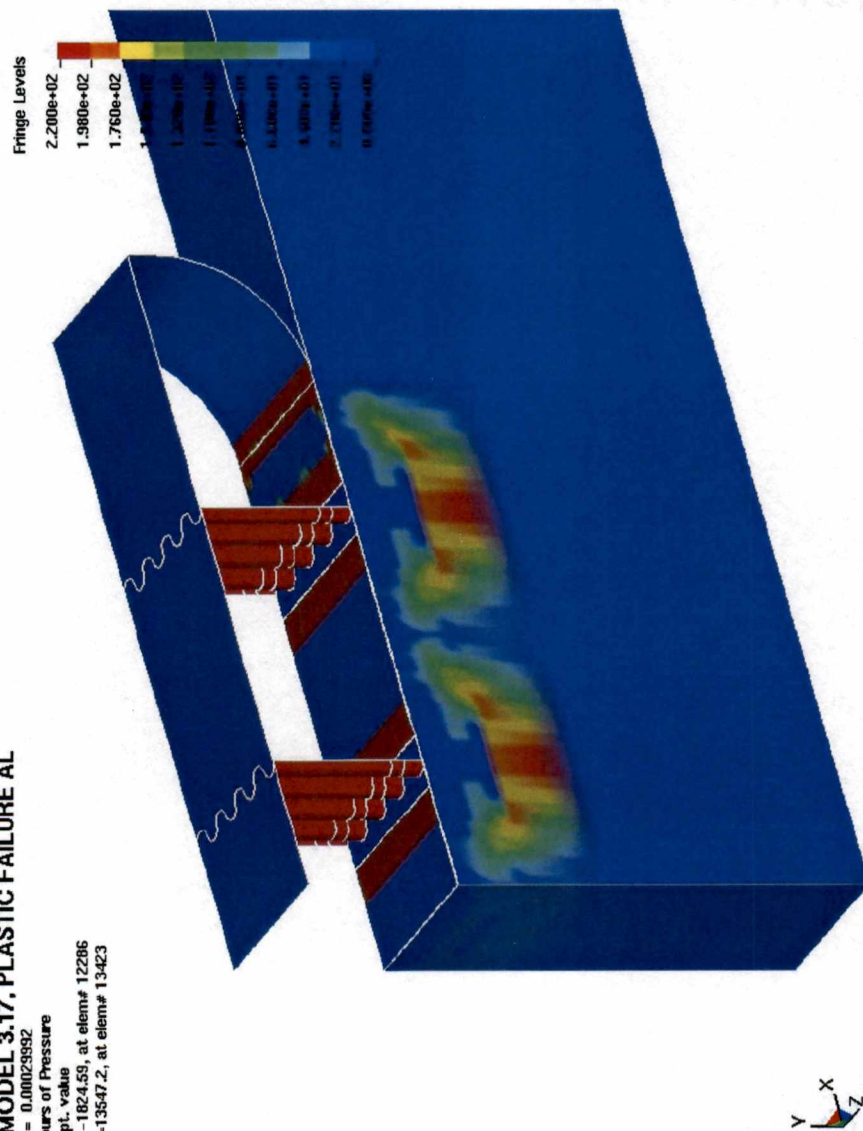
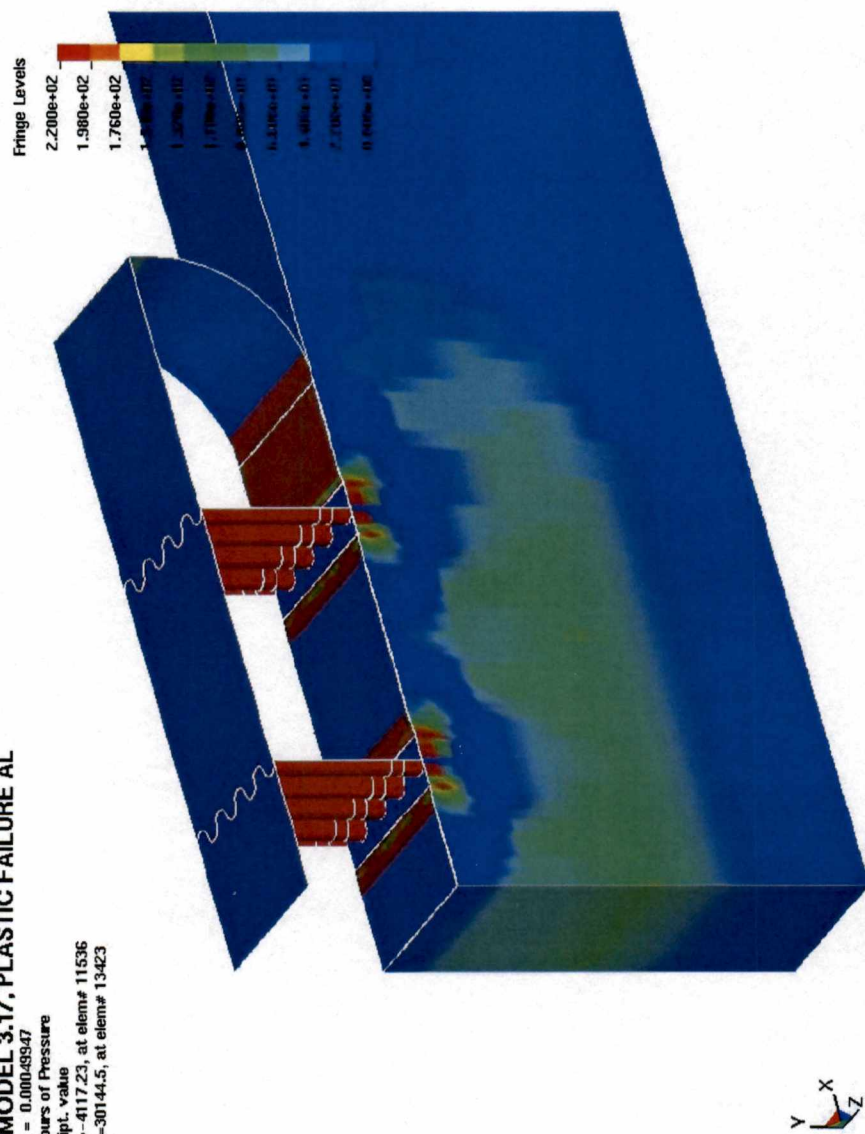


Figure 4.4.1.12 Pressure at Time $t=0.0003\text{sec}$, Model 3.17

3D MODEL 3.17, PLASTIC FAILURE AL

Time = 0.00049347
 Contours of Pressure
 max ip1. value
 min=-4117.23, at elem# 11536
 max=30144.5, at elem# 13423



Note that 0.2 milliseconds later, the two pressure waves have propagated further and merged, while another pair of pressure waves is beginning to form below the two beam footings. This oscillatory contact pressure is responsible for the oscillatory accelerations. Further, note that to this time, the skin has had little to no affect. The skin behavior becomes significant only at later times.

Figure 4.4.1.13 Pressure at Time $t=0.0005\text{sec}$, Model 3.17

3D MODEL 4.7, COMPOSITE FAILURE
Time = 0.0050003

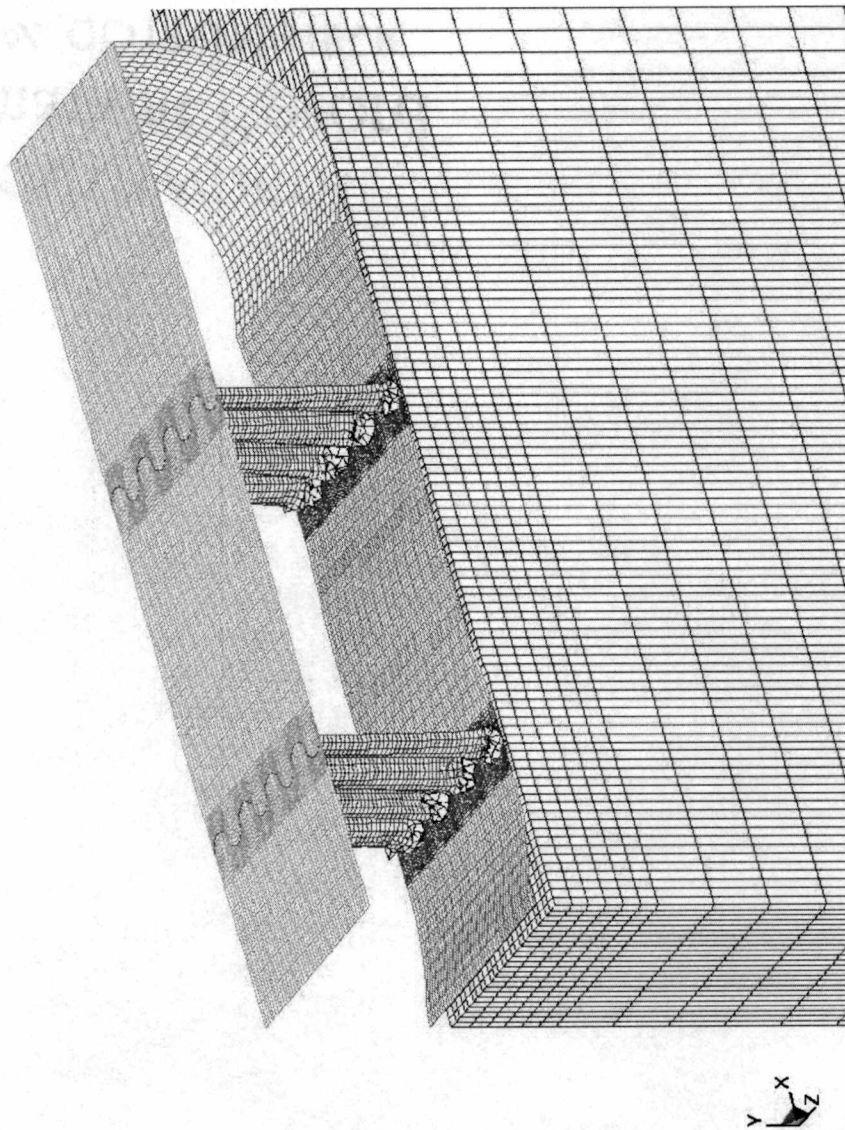


Figure 4.4.2.1 Model 4.7 at time $t=0.005$ sec

Rotorcraft substructure consists of two sine wave web beams, the rotorcraft floor, and the skin. Impacted body is rigid material representing a hard surface. Bodies are not initially touching. Rotorcraft beams and skin employ material type 55 representing unidirectional carbon epoxy composite. Rotorcraft floor is rigid. Initiator located near bottom. Visually very similar to figures 4.4.1.1 through 4.4.1.3. Model 4.7 is identical to model 3.16 except for beam and skin materials and thickness.

In comparison with figure 4.4.1.4 note the slightly higher first peak acceleration near .15 milliseconds, the second high peak near 1 millisecond, and the slightly higher sustained acceleration.

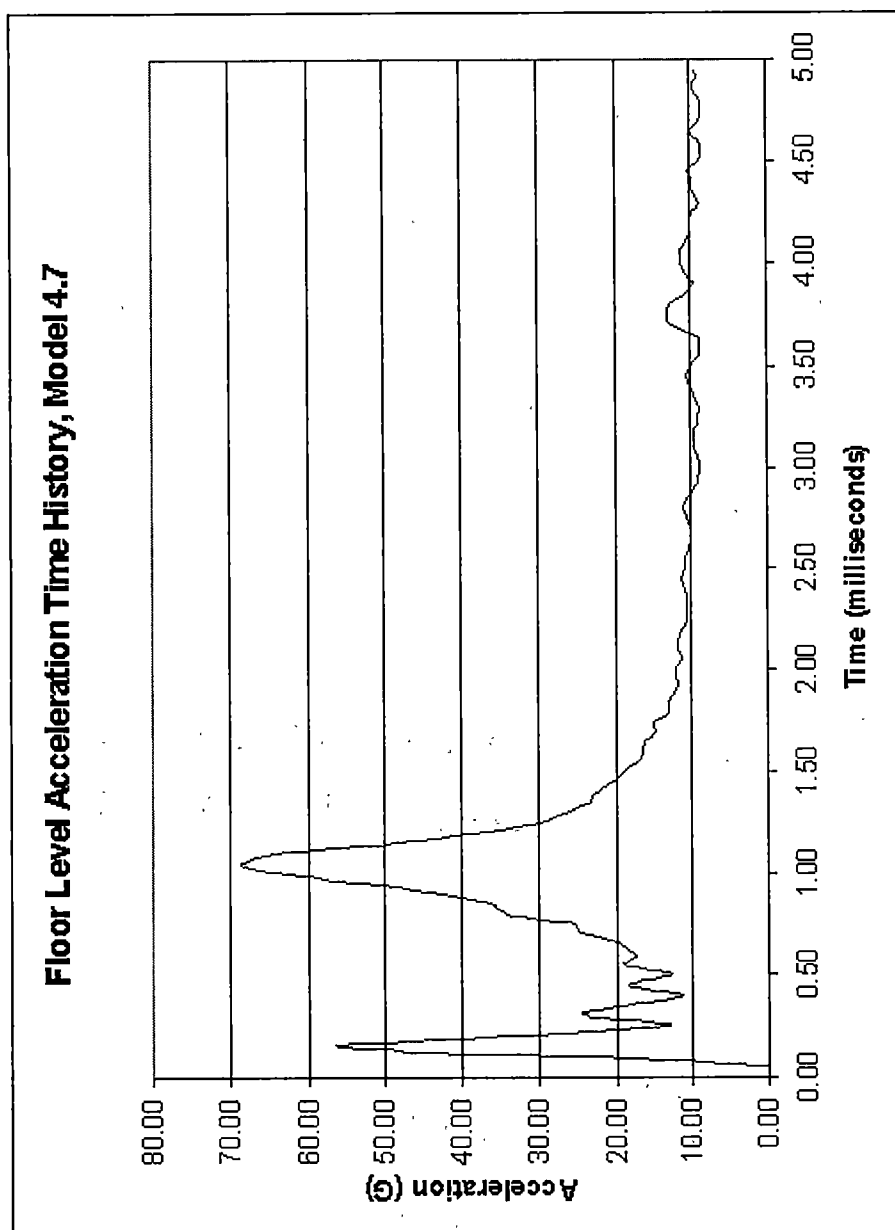


Figure 4.4.2.2 Floor Level Acceleration Time History, Model 4.7

Peak value of 10964 lbf-in represents approximately 20.5% of the total of 53477 lbf-in of kinetic energy in the structure at impact. This is significantly better than model 3.16, figure 4.4.1.5, and is due both to the slightly higher sustained acceleration and the existence of the second high acceleration peak, which was absent in model 3.16.

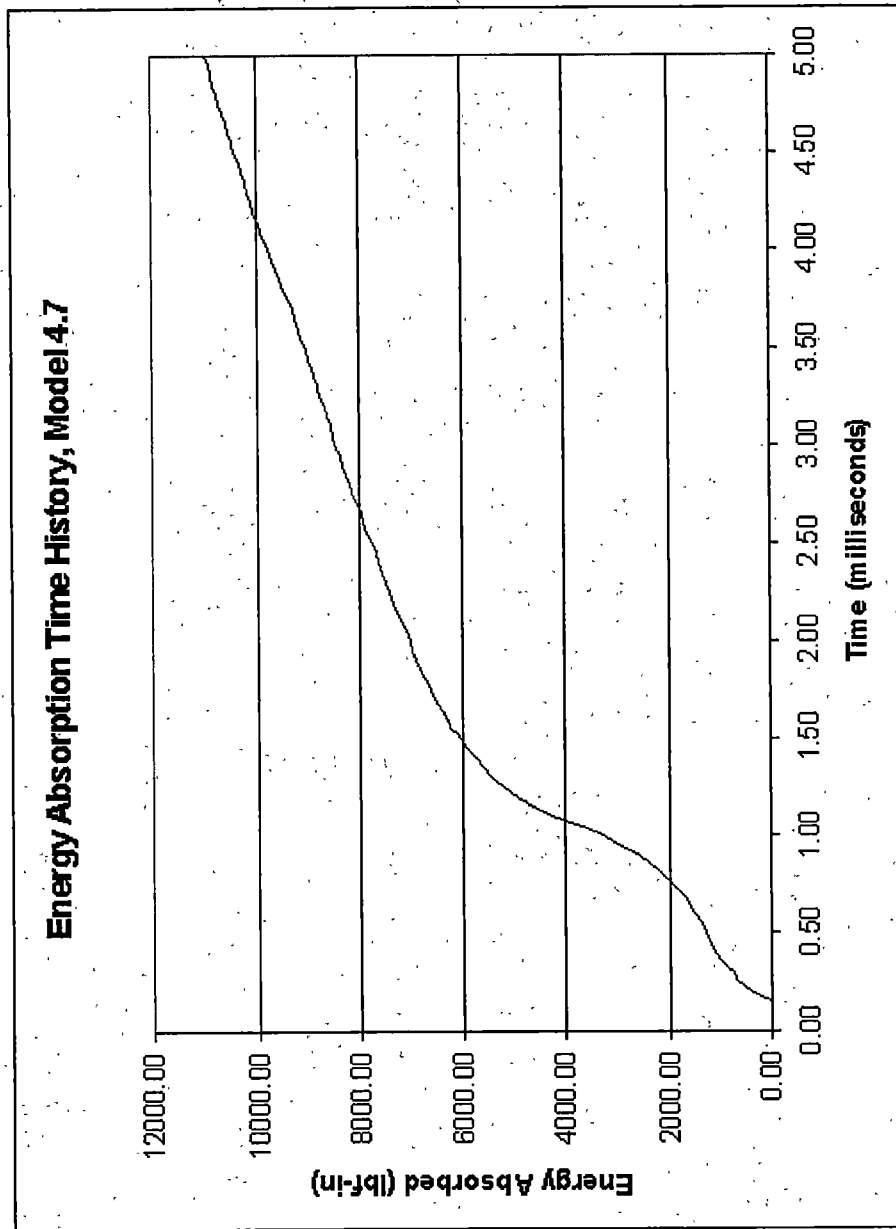


Figure 4.4.2.3 Energy Absorption Time History, Model 4.7

Model is a composite rotorcraft structure impacting water. Null material with a linear polynomial EOS was employed to model the water. Except for the impacted material, model is identical to model 4.7. Skin is composed of two lamina of unidirectional carbon epoxy composite, one running parallel to the sine wave beams and one perpendicular to them. Visual model behavior very similar to figures 4.4.1.6 through 4.4.1.8. Comparing this plot to figure 4.4.1.9, the early accelerations (up to 2.5 milliseconds) are somewhat lower. Later accelerations, which are influenced by skin behavior, are higher than figure 4.4.1.9. The higher stiffness of the composite skin appears to influence this acceleration level.

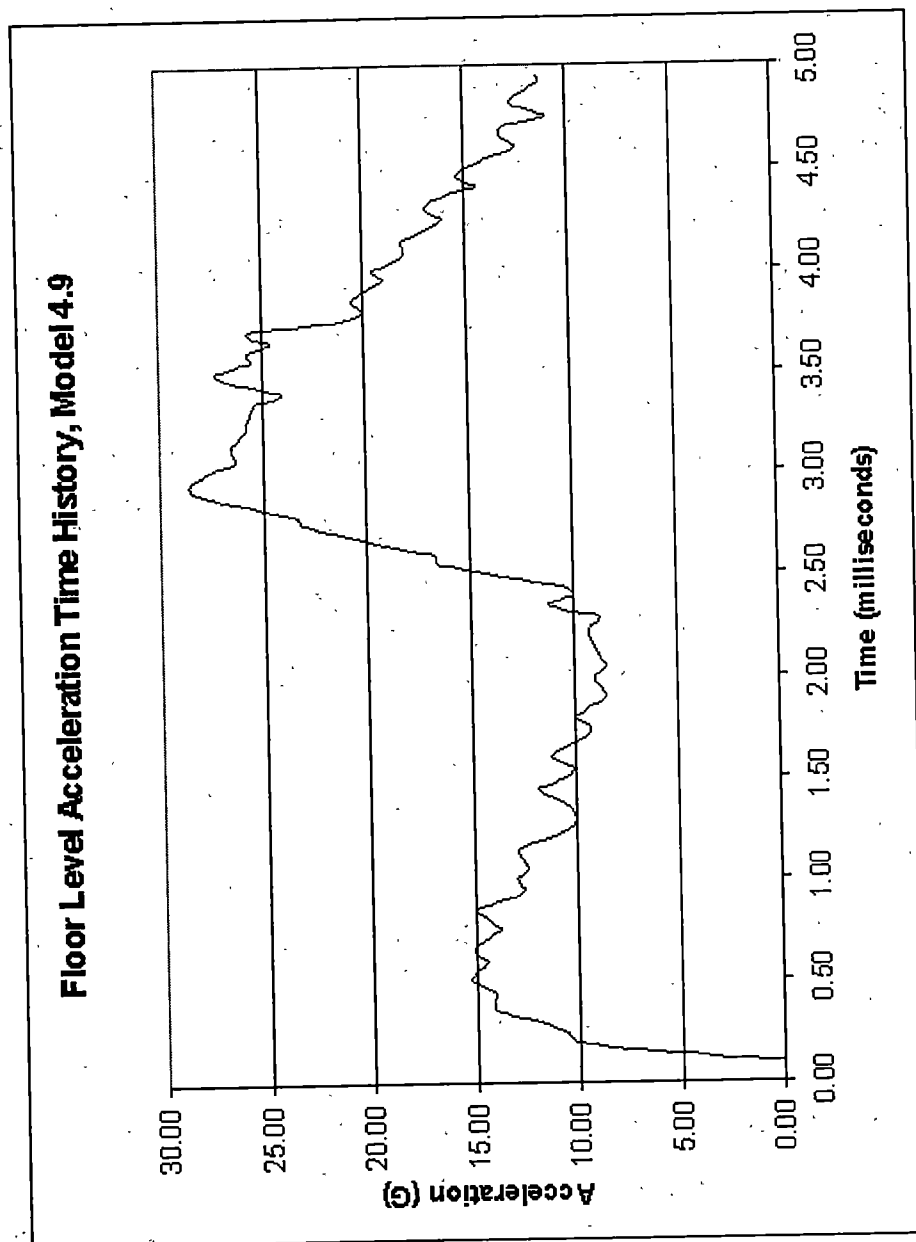


Figure 4.4.2.4 Floor Level Acceleration Time History, Model 4.9

Comparing this figure to model 3.17, figure 4.4.1.10, the overall energy absorption is nearly the same. The differences in acceleration wash out. Again, approximately 20% of the total energy has been absorbed.

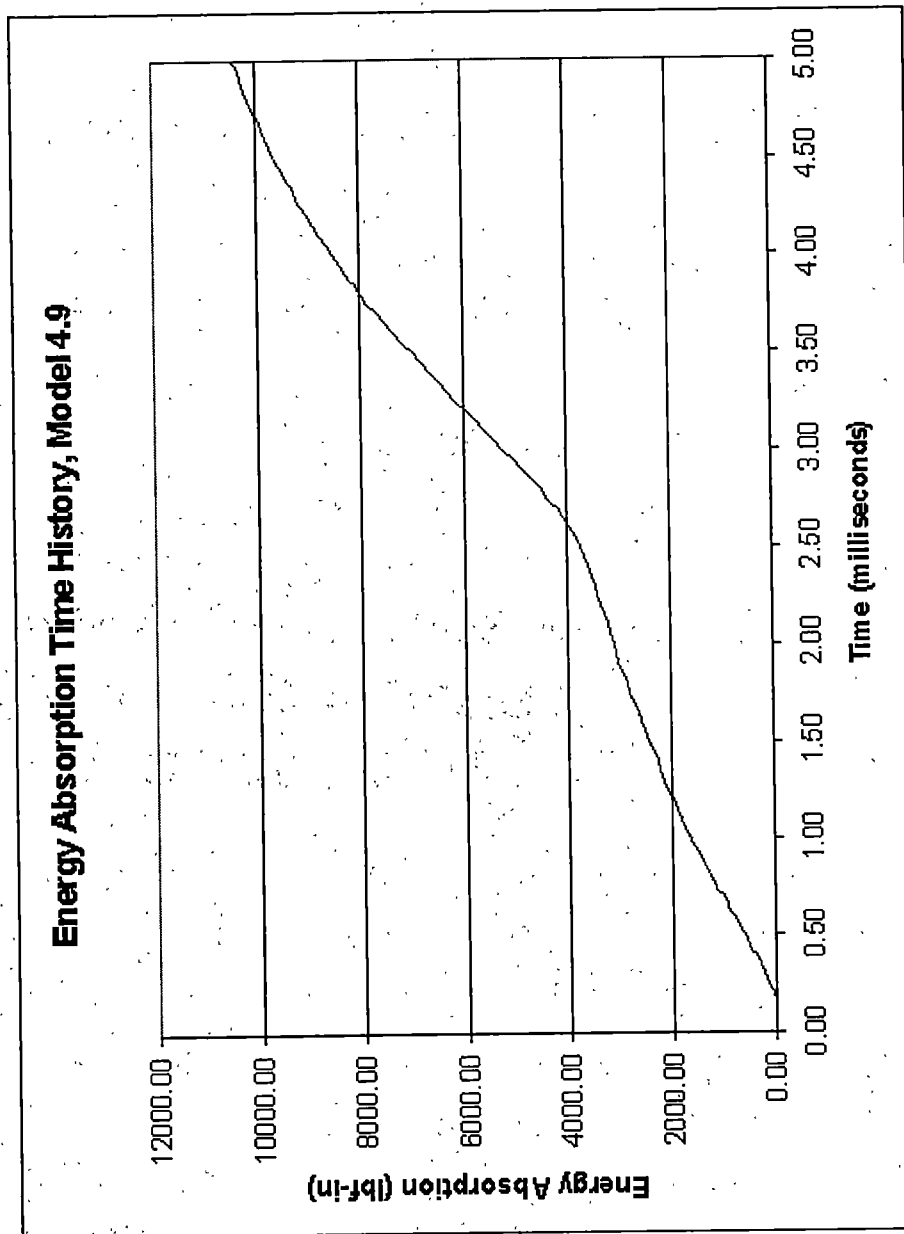


Figure 4.4.2.5 Energy Absorption Time History, Model 4.9

Compared with figure 4.4.2.4, not the nearly identical behavior except for some slight differences in the accelerations between 3.1 and 4 milliseconds. As the skin is different between these models, and the skin has some influence on these later accelerations, the difference is in the expected region. However, the differences are very small.

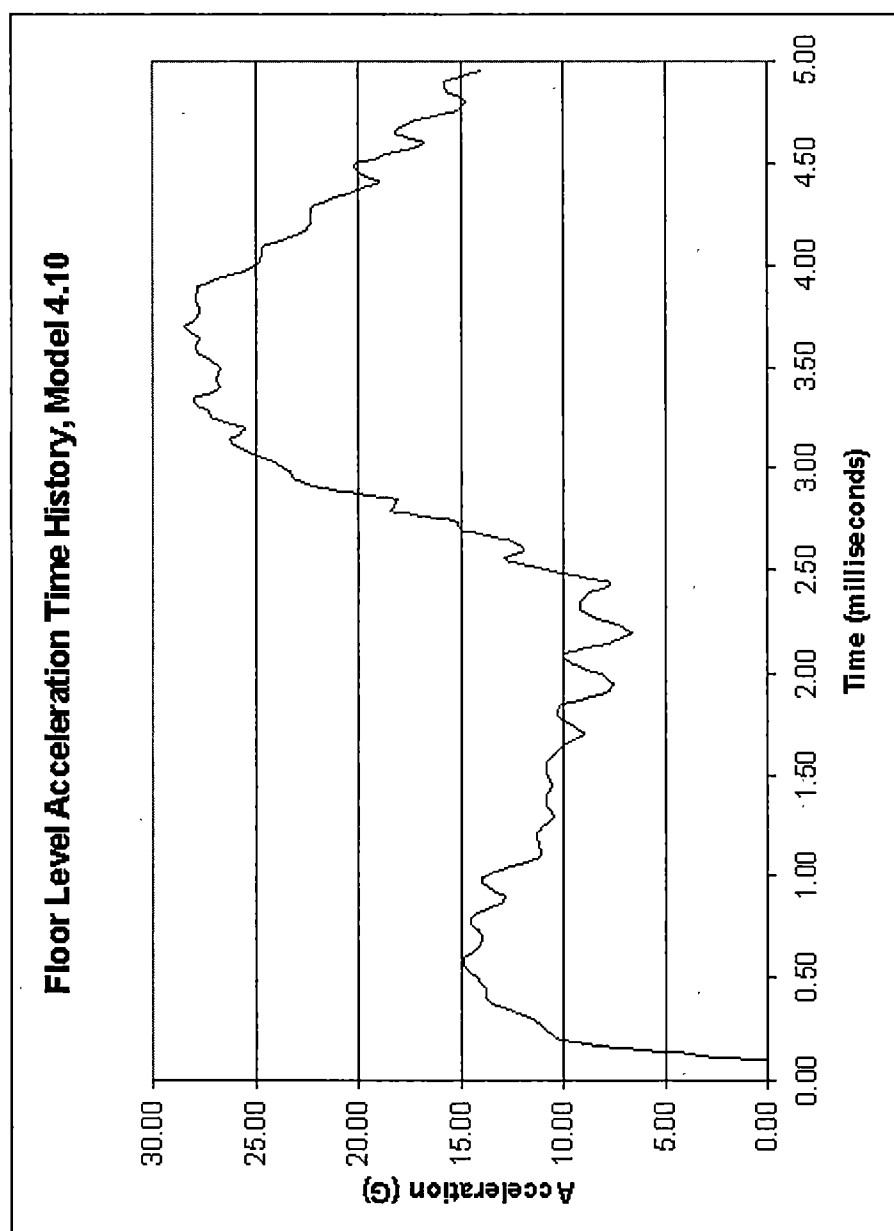


Figure 4.4.2.6 Floor Level Acceleration Time History, Model 4.10

Appendix B - Tables

Table 2.0.1 Summary of Mil-Std-1290 A

Condition Number	Impact Direction	Impacted Surface	Velocity Change
1	Longitudinal Cockpit	Rigid Vertical Surface	20 ft/sec
2	Longitudinal Cabin	Rigid Vertical Surface	40 ft/sec
3	Vertical With Lowered Landing Gear	Rigid Horizontal Surface	42 ft/sec
	Vertical with Raised Landing Gear	Rigid Horizontal Surface	26 ft/sec
4	Lateral, Type I	Rigid Horizontal Surface	25 ft/sec
5	Lateral Type II	Rigid Horizontal Surface	30 ft/sec
6	Combined High Angle Vertical	Rigid Horizontal Surface	42 ft/sec Vertical, 27 ft/sec Horizontal
7	Combined Low Angle Vertical	Plowed Soil	14 ft/sec Vertical, 100 ft/sec Horizontal

Table 3.4.1 Summary of Linear Polynomial EOS Parameters for Simulation of Water

Name	Value	Units
C0	0	psi
C1	33,000	Dimensionless
C2	0	Dimensionless
C3	0	Dimensionless
C4	0	Dimensionless
C5	0	Dimensionless
C6	0	Dimensionless
E0	1×10^{-6}	Dimensionless
V0	1	Dimensionless

Table 3.4.2 Summary of Gruneisen EOS Parameters for Simulation of Water

Parameter	Name	Value	Units
C (Speed of Sound)	SP	57.53×10^5	in/sec
Gruneisen Gamma	Gamma	0.280	Dimensionless
S1	S1	1.75	Dimensionless
S2	S2	0	Dimensionless
S3	S3	0	Dimensionless
A	SA	0	Dimensionless
Initial Energy	E0	1×10^{-6}	Dimensionless
Initial Relative Volume	V0	1	Dimensionless

Table 3.4.3 Summary of 2024-T4 Aluminum Alloy Material Parameters

Parameter	Name	Value	Units
Youngs Modulus	E	10.501×10^6	psi
Yield Strength	sigy	47.0×10^3	psi
Ultimate Strain	fs	0.200	in/in
Plastic Modulus	etan	1×10^5	psi

Table 3.4.4 Summary of Unidirectional Carbon Epoxy Composite Material**Parameters**

Parameter	Name	Value	Units
Youngs Modulus, Fiber Direction	EA	20.6×10^6	psi
Youngs Modulus, Transverse Direction	EB	1.50×10^6	psi
Poissons Ratio, Transverse-Fiber Direction	PRBA	0.02	dimensionless
Shear Modulus, Fiber-Transverse Direction	GAB	1.04×10^6	psi
Shear Modulus, Transverse-Transverse Direction	GBC	1.04×10^6	psi
Shear Modulus, Transverse-Fiber Direction	GCA	1.04×10^6	psi
Ultimate Tensile Strength, Fiber Direction	XT	330×10^3	psi
Ultimate Tensile Strength, Transverse Direction	YT	8.3×10^3	psi
Ultimate Compressive Strength, Fiber Direction	XC	209×10^3	psi
Ultimate Compressive Strength, Transverse Direction	YC	33×10^3	psi
Shear Strength, Fiber-Transverse Direction	SC	10.3×10^3	psi

Table 3.4.5 Summary of [0°/90°] Laminated Carbon Epoxy Composite Material

Parameters

Parameter	Name	Value	Units
Youngs Modulus, Fiber Direction	EA	11.05×10^6	psi
Youngs Modulus, Transverse Direction	EB	11.05×10^6	psi
Poissons Ratio, Transverse-Fiber Direction	PRBA	0.27	dimensionless
Shear Modulus, Fiber-Transverse Direction	GAB	1.04×10^6	psi
Shear Modulus, Transverse-Transverse Direction	GBC	1.04×10^6	psi
Shear Modulus, Transverse-Fiber Direction	GCA	1.04×10^6	psi
Ultimate Tensile Strength, Fiber Direction	XT	169.15×10^3	psi
Ultimate Tensile Strength, Transverse Direction	YT	169.15×10^3	psi
Ultimate Compressive Strength, Fiber Direction	XC	121×10^3	psi
Ultimate Compressive Strength, Transverse Direction	YC	121×10^3	psi
Shear Strength, Fiber-Transverse Direction	SC	10.3×10^3	psi

Table 3.4.6 Summary of [0°/90°] Laminated Kevlar Epoxy Composite Material**Parameters**

Parameter	Name	Value	Units
Youngs Modulus, Fiber Direction	EA	6.7×10^6	psi
Youngs Modulus, Transverse Direction	EB	6.7×10^6	psi
Poissons Ratio, Transverse-Fiber Direction	PRBA	0.34	dimensionless
Shear Modulus, Fiber-Transverse Direction	GAB	0.31×10^6	psi
Shear Modulus, Transverse-Transverse Direction	GBC	0.31×10^6	psi
Shear Modulus, Transverse-Fiber Direction	GCA	0.31×10^6	psi
Ultimate Tensile Strength, Fiber Direction	XT	94.6×10^3	psi
Ultimate Tensile Strength, Transverse Direction	YT	94.6×10^3	psi
Ultimate Compressive Strength, Fiber Direction	XC	35.95×10^3	psi
Ultimate Compressive Strength, Transverse Direction	YC	35.95×10^3	psi
Shear Strength, Fiber-Transverse Direction	SC	7.1×10^3	psi

Vita

Stephan Wintner was born in New Jersey in 1975. During his childhood he moved from New Jersey to Alabama, Illinois, and then to Pennsylvania, attending a number of public and private schools. After graduating from Central Bucks West High School, in Doylestown Pennsylvania, he attended RPI (Rennselaer Polytechnic Institute) in Troy New York and graduated in December of 1997 with a Bachelors Degree in Mechanical Engineering. He worked for Pratt & Whitney in East Hartford and Middletown Connecticut from March of 1998 to August of 2000. At that point he moved to Tullahoma, Tennessee to attend the University of Tennessee's Space Institute full time. During his time at UTSI, he was supported by a NASA space grant and a Morris Simon Fellowship. He has accepted a position as a design engineer with Motoren und Turbo Union's Aero Engine Design subsidiary in Rock Hill Connecticut and will be starting work there in January of 2002.